

## Double hits with bioactive nanozyme based on cobalt-doped nanoglass for acute and diabetic wound therapies through anti-inflammatory and pro-angiogenic functions

Nandin Mandakhbayar<sup>a,b,1</sup>, YunSeong Ji<sup>a,b,1</sup>, Ahmed El-Fiqi<sup>c</sup>, Kapil D. Patel<sup>a,b,d</sup>, Dong Suk Yoon<sup>a,e</sup>, Khandmaa Dashnyam<sup>a,b,f</sup>, Oyunchimeg Bayaraa<sup>a,b,f</sup>, Gangshi Jin<sup>a,b</sup>, Khaliunsarnai Tsogtbaatar<sup>a,b,f</sup>, Tae-Hyun Kim<sup>a,b,g</sup>, Jung-Hwan Lee<sup>a,b,h,i,j,k,\*\*</sup>, Hae-Won Kim<sup>a,b,h,i,j,k,\*</sup>

<sup>a</sup> Institute of Tissue Regeneration Engineering (ITREN), Dankook University, Cheonan, 31116, Republic of Korea

<sup>b</sup> Department of Nanobiomedical Science and BK21 PLUS NBM Global Research Center for Regenerative Medicine, Dankook University, Cheonan, 31116, Republic of Korea

<sup>c</sup> Glass Research Department, National Research Centre, Cairo, 12622, Egypt

<sup>d</sup> School of Cellular and Molecular Medicine (CMM), University of Bristol, Bristol, BS8 1TD United Kingdom

<sup>e</sup> Department of Biomedical Science, Hwasung Medi-Science University, Hwaseong-Si 18274, Gyeonggi-Do, Republic of Korea

<sup>f</sup> Drug Research Institute, Mongolian University of Pharmaceutical Sciences, Ulaanbaatar 14250, Mongolia

<sup>g</sup> R&D Center, TE Bios, Osong, Republic of Korea

<sup>h</sup> Department of Biomaterials Science, School of Dentistry, Dankook University, Cheonan, 31116, Republic of Korea

<sup>i</sup> Mechanobiology Dental Medicine Research Center, Dankook University, Cheonan, 31116, Republic of Korea

<sup>j</sup> UCL Eastman-Korea Dental Medicine Innovation Centre, Dankook University, Cheonan, 31116, Republic of Korea

<sup>k</sup> Cell & Matter Institute, Dankook University, Cheonan 31116, Republic of Korea

### ARTICLE INFO

#### Keywords:

Diabetic wound  
Nanozyme  
Anti-inflammation  
Angiogenesis  
Therapeutic materials

### ABSTRACT

Regeneration of pathological wounds, such as diabetic ulcers, poses a significant challenge in clinical settings, despite the widespread use of drugs. To overcome clinical side effects and complications, drug-free therapeutics need to be developed to promote angiogenesis while overcoming inflammation to restore regenerative events. This study presents a novel bioactive nanozyme based on cobalt-doped nanoglass (namely, CoNZ), which exhibits high enzymatic/catalytic activity while releasing therapeutic ions. Cobalt oxide “Co<sub>3</sub>O<sub>4</sub>” tiny crystallites produced *in situ* through a chemical reaction with H<sub>2</sub>O<sub>2</sub> within CoNZ nanoparticles play a crucial role in scavenging ROS. Results showed that CoNZ-treatment to full-thickness skin wounds in mice significantly accelerated the healing process, promoting neovascularization, matrix deposition, and epithelial lining while reducing pro-inflammatory signs. Notably, CoNZ was highly effective in treating pathological wounds (streptozotocin-induced diabetic wounds). Rapid scavenging of ROS by CoNZ and down-regulation of pro-inflammatory markers while up-regulating tissue healing signs with proliferative cells and activated angiogenic factors contributed to the observed healing events. *In vitro* experiments involving CoNZ-cultures with macrophages and endothelial cells exposed to high glucose and ROS-generating conditions further confirmed the effectiveness of CoNZ. CoNZ-promoted angiogenesis was attributed to the release of cobalt ions, as evidenced by the comparable effects of CoNZ-extracted ionic medium in enhancing endothelial migration and tubule formation via activated HIF-1 $\alpha$ . Finally, we compared the *in vivo* efficacy of CoNZ with the clinically-available drug deferoxamine. Results demonstrated that CoNZ was as effective as the drug in closing the diabetic wound, indicating the potential of CoNZ as a novel drug-free therapeutic approach.

Peer review under responsibility of KeAi Communications Co., Ltd.

\* Corresponding author. Institute of Tissue Regeneration Engineering (ITREN), Dankook University, Cheonan, 31116, Republic of Korea.

\*\* Corresponding author. Institute of Tissue Regeneration Engineering (ITREN), Dankook University, Cheonan, 31116, Republic of Korea.

E-mail addresses: [ducious@gmail.com](mailto:ducious@gmail.com) (J.-H. Lee), [kimhw@dku.edu](mailto:kimhw@dku.edu) (H.-W. Kim).

<sup>1</sup> These authors contributed equally to this work.

<https://doi.org/10.1016/j.bioactmat.2023.08.014>

Received 27 May 2023; Received in revised form 27 July 2023; Accepted 13 August 2023

2452-199X/© 2023 The Authors. Publishing services by Elsevier B.V. on behalf of KeAi Communications Co. Ltd. This is an open access article under the CC BY-NC-ND license (<http://creativecommons.org/licenses/by-nc-nd/4.0/>).

## 1. Introduction

The regeneration of pathological wounds, such as those associated with diabetic ulcers, vascular deficits, hypertension, and chronic kidney disease, poses a significant challenge in clinical settings [1,2]. They are commonly accompanied by severe inflammation, including excessive production of reactive oxygen species (ROS) and the presence of pro-inflammatory cytokines [3–6]. These events damage surrounding cells and tissues, creating a positive feedback loop that exacerbates chronic inflammation and functional impairment. Furthermore, pathological wounds often exhibit poor vascularization, which restricts the delivery of oxygen and nutrients to the wound site, complicating the healing process and contributing to the persistence of chronic wounds [7,8]. To successfully heal pathological wounds and improve patient outcomes, it is crucial to address these challenges and develop effective strategies to reduce inflammation while improving neovascularization.

One of the common pathological conditions that cause delayed wound healing is diabetes mellitus (DM), which is characterized by elevated blood sugar levels resulting from impaired insulin secretion or reception, crucial for regulating blood sugar. Diabetic wounds are distinguished by severe inflammation accompanied by heightened oxidative stress, which induces chronic inflammation and hinders adequate angiogenesis, thereby significantly delaying the healing process [6,9–12]. Consequently, diabetic wounds incur substantial medical expenses, compromise the quality of life, and may even lead to fatality. For the treatment of pathological wounds including diabetic wounds, medications have been extensively employed in clinical settings, each targeting specific aspects of the healing process [13,14]. However, these medications often give rise to side effects and complications, including allergic reactions, increased drug resistance among pathogens, and interference with other medications [15]. To address these limitations, more advanced therapeutic approaches have emerged, involving the utilization of bioactive molecules, engineered cells, and functional biomaterials [16–19].

In particular, biomaterials offer a promising solution to address the challenges of diabetic wounds. In addition to delivering drugs to the targeted tissues, biomaterials themselves can have therapeutic effects, eliminating the need for drug-based approaches. Recent studies have demonstrated the therapeutic potential of biomaterials. Among the formulations of biomaterials, ionic-doped bioactive glasses have been shown to release ions with anti-inflammatory and pro-angiogenic properties, and they can also guide stem cell lineage [20–25]. For example, when doped with copper or zinc, bioactive glasses have demonstrated the efficacy in promoting angiogenesis, thereby accelerating the wound healing process [26,27]. Another promising approach recently explored is the nanozymes, which are nanomaterials with enzymatic actions that can scavenge ROS and alleviate the inflammatory environment of cells. Examples of nanozymes include cerium oxide, ultrafine copper oxide, silver and cobalt oxide [10,20,27–31]. These biomaterial-based approaches have the potential to provide safe and effective treatments for pathological wounds.

With these in mind, here we propose a biomaterial-based drug-free therapeutic approach for pathological wound, particularly diabetic skin wound. We present a novel bioactive nanozyme based on cobalt-doped nanoglass (namely, CoNZ), which possesses high enzymatic and catalytic ('anti-inflammatory') capability while releasing therapeutic ('pro-angiogenic') ions [32–35]. Among other ions that can be doped to nanoglass, cobalt is particularly noteworthy because we discovered the *in situ* production of cobalt oxide "Co<sub>3</sub>O<sub>4</sub>" tiny crystallites through chemical reactions with ROS (mainly H<sub>2</sub>O<sub>2</sub>) within the CoNZ network, which proven to play a decisive role in scavenging various ROS and inhibiting inflammatory cascade. Furthermore, cobalt ions released from CoNZ show specific therapeutic properties of promoting angiogenesis with increased endothelial migration and tubule formation. We demonstrate the efficacy of CoNZ first in a full-thickness skin wound model and then in a streptozotocin-induced diabetic wound model in

mice, by in-depth analysis of inflammatory signs, neovascularization, matrix deposition, and epithelial lining. The currently developed CoNZ is considered to represent a promising drug-free nanotherapeutic platform for healing pathological wounds.

## 2. Results and discussion

### 2.1. Synthesized CoNZ bioactive nanozyme holds enzymatic and catalytic capacity with therapeutic ionic release

In this study, we synthesized cobalt ion-doped bioactive nanozyme (CoNZ) through a modified sol-gel method, employing poly(ethylene glycol) as a structure template under an alkaline condition. High-resolution scanning electron microscopy (HR-SEM) images showed CoNZ particles with an average diameter of 54.8 (±5) nm (Fig. 1A). CoNZ displayed a mesoporous structure with a specific surface area of 126.8 m<sup>2</sup>/g, an average mesopore size of 6.2 nm, and a pore volume of 0.158 cm<sup>3</sup>/g, akin to the characteristics of undoped pure bioactive nanoglass (BGn) (supplementary data, Fig. S1).

Notably, we observed various enzymatic and catalytic properties of CoNZ, as measured by its superoxide dismutase (SOD) activity, peroxidase activity, catalase activity, and oxygen generation capacity. We assessed the SOD activity of CoNZ through a colorimetric assay (Fig. 1B), given its crucial role in protecting mitochondrial tissues from superoxide radicals that are highly toxic to cells. The SOD mimetic activity of CoNZ was found to be nearly 30 times higher than that of the BGn control, based on its effective scavenging of superoxide anion O<sub>2</sub><sup>-</sup>. We used an optimal doping level of 5% Co in the nanoglass composition, which showed the highest SOD activity among the samples with different Co-doping concentrations (supplementary data, Fig. S2). The peroxidase mimetic activity of CoNZ was also significantly enhanced (Fig. 1C), given that the decomposition of H<sub>2</sub>O<sub>2</sub> into H<sub>2</sub>O is highly beneficial in protecting cells from oxidative stress. The colorimetric TMB assay showed a rapid increase in absorbance in a CoNZ dose-dependent manner, in contrast to the 0.5 M H<sub>2</sub>O<sub>2</sub> control solution (supplementary data, Fig. S3). Furthermore, CoNZ exhibited significantly higher catalase activity than BGn (Fig. 1D). These capabilities of CoNZ to scavenge radical species were found to be closely related to the oxygen generation reaction. We measured the kinetic conversion activity of CoNZ through current density, for oxygen evolution reaction (OER) and oxygen reduction reaction (ORR), which also corresponds to the ROS scavenging activity. CoNZ showed higher current density for OER than BGn with little difference in ORR, with the highest activity observed at 5% Co-doping (Fig. 1E and F, and supplementary data, Fig. S4).

Next, we sought to find the material mechanism of how CoNZ possesses such excellent enzymatic and catalytic activities. For this, we first examined the crystalline structure of both BGn and CoNZ nanoglass particles by X-ray diffraction (XRD) (Fig. 1G). Both samples showed an amorphous pattern characteristic of silicate-based glasses. However, upon treatment with H<sub>2</sub>O<sub>2</sub>, crystalline peaks indexed as "Co<sub>3</sub>O<sub>4</sub>" appeared in CoNZ (as also observed in the Co<sub>3</sub>O<sub>4</sub> sample prepared for comparison, shown in supplementary data, Fig. S5), indicating that CoNZ reacted with H<sub>2</sub>O<sub>2</sub> to produce Co<sub>3</sub>O<sub>4</sub>, which likely plays a key role in the observed enzymatic activity. We further analyzed the chemical binding of elements associated with the reaction of CoNZ with H<sub>2</sub>O<sub>2</sub> by X-ray photoelectron spectroscopy (XPS). Among the elements revealed from a survey scan (Ca, Si, O, and Co), we focused on Co, analyzing it in-depth by deconvolution of peaks at a narrow scan (Fig. 1H, and supplementary data in Fig. S6). We observed clear Co 2p<sub>1/2</sub> and Co 2p<sub>3/2</sub> peaks for both nanoglass samples, indicative of different cobalt species within the glass structure with corresponding binding energies reported to be ~778 eV (Co), ~781 eV (CoO or Co(OH)<sub>2</sub>), and ~785 eV (Co<sub>3</sub>O<sub>4</sub>), implying the potentially variable coordinated status of cobalt within the glass structure. Notably, the satellite peak at ~797 eV related to Co (II) was substantially reduced in the CoNZ activated sample, indicating that Co (III) species became more dominant due to the produced Co<sub>3</sub>O<sub>4</sub>

( $I_{\text{main}}/I_{\text{satellite}}$  in CoNZ activated = 3.24, vs.  $I_{\text{main}}/I_{\text{satellite}}$  in CoNZ = 2.6). Further examination of the CoNZ activated sample from transmission electron microscopy (TEM) images revealed the presence of tiny (~a few nm sized) nano-crystallites indicative of  $\text{Co}_3\text{O}_4$ , distributed in the CoNZ network (Fig. 1I). The  $\text{Co}_3\text{O}_4$  is believed to form *in situ* through the chemical reaction with  $\text{H}_2\text{O}_2$  and plays a key role in scavenging various ROS (as depicted in Fig. 1J). Indeed, we found that cobalt oxide with Co (III) oxidation status has a higher oxygen generation capacity than the oxide with Co (II) status, as tested using different cobalt oxide materials (supplementary data, Fig. S7).

The release of ions from CoNZ was measured at 37 °C by inductively coupled plasma-atomic emission spectroscopy (ICP-AES) (Fig. 1K).

Calcium, silicate, and cobalt ions were released over a period of 28 days. The release of calcium and silicate ions was rapid during the first 7 days, followed by a slower release rate until 28 days, whereas the release of cobalt ions was relatively constant throughout the test period. The release of calcium and silicate ions from CoNZ was similar to that of BGn (supplementary data, Fig. S8), except for the cobalt ion release, which was approximately 100 ppm over 28 days. The release rate of cobalt ions (ppm/day) was then plotted over time (Fig. 1L), which revealed a release rate of approximately 3.4 ppm per day. The release of calcium and silicate ions from CoNZ is expected to promote angiogenic stimulation, as demonstrated in previous studies with Co-undoped BGn, which exhibited comparable levels of silicate and calcium release

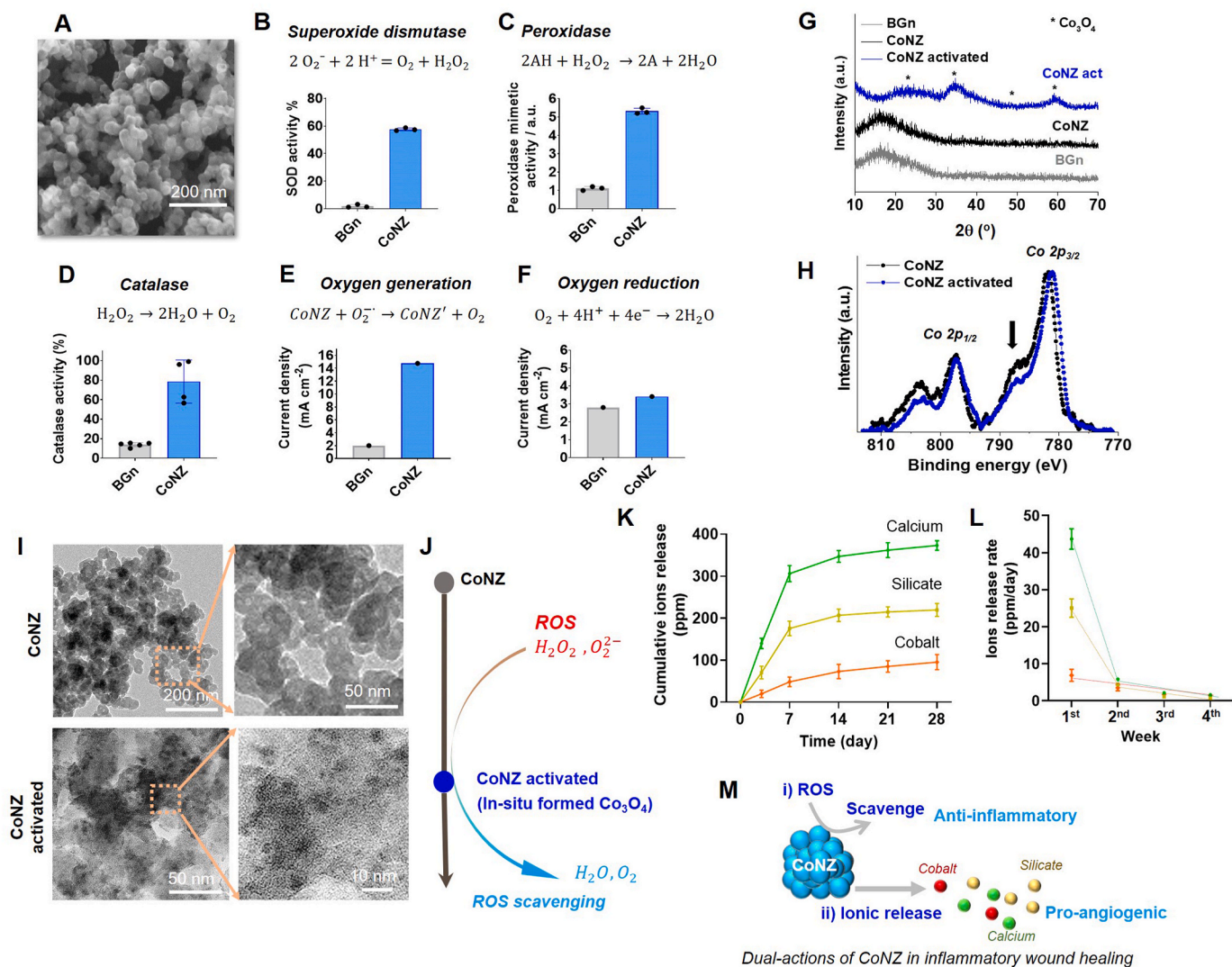


**Fig. 1.** Synthesized CoNZ bioactive nanozyme with excellent enzymatic and catalytic capacity and therapeutic ionic release. (A) High-resolution scanning electron microscopy (HR-SEM) image of CoNZ particles with an average diameter of 54.8 nm. (B–F) Enzymatic and catalytic properties of CoNZ in comparison with pure (Co-undoped) nanoglass BGn; CoNZ exhibited significantly enhanced superoxide dismutase (SOD) activity (B), peroxidase mimetic activity (C), and oxygen generation capacity (D–E) compared to BGn; however, oxygen reduction capacity (F) was similar for both nanoparticles. (G) X-ray diffraction (XRD) patterns of samples showing that both BGn and CoNZ are amorphous silicate-based glasses, but the CoNZ activated sample exhibited additional crystalline peaks of  $\text{Co}_3\text{O}_4$ . (H) X-ray photoelectron spectroscopy (XPS) analysis of samples, particularly the Co element at a narrow scan; Co 2p<sub>1/2</sub> and Co 2p<sub>3/2</sub> peaks were well observed for both samples, and the satellite peak at ~786 eV (arrowed) related with  $\text{Co}^{2+}$  was substantially reduced in CoNZ activated one, indicating  $\text{Co}^{3+}$  due to the produced  $\text{Co}_3\text{O}_4$  became more dominant. (I) Transmission electron microscopy (TEM) images of CoNZ and CoNZ activated samples, showing the existence of tiny (~a few nm sized) nano-crystallites (deemed to be  $\text{Co}_3\text{O}_4$ ) only in the CoNZ activated case. (J) Illustration showing the possible roles of CoNZ in scavenging reactive oxygen species (ROS). (K) Cumulative release of calcium, silicate, and cobalt ions from CoNZ, as measured by inductively coupled plasma-atomic emission spectroscopy (ICP-AES) for up to 28 days. (L) Release rate (ppm/day) of ions from CoNZ plotted on a weekly basis. (M) Schematic showing the dual-actions of CoNZ in healing inflammatory wounds; CoNZ can act as an anti-inflammatory agent by scavenging ROS and a pro-angiogenic agent by releasing ions, both of which can be beneficial for wound healing in highly inflammatory conditions.

[36–38]. Additionally, Co ions have been shown to promote angiogenic functions of cells by activating hypoxic inducible factor-1 $\alpha$  (HIF-1 $\alpha$ ) [39–41].

Taken together, the effects of CoNZ are considered two-fold; on the one hand, the enzymatic activity that scavenges ROS under high oxidative conditions, and on the other hand, the angiogenic stimulation

through released ions, both of which are expected to be advantageous for wound healing in highly inflammatory conditions (as depicted in Fig. 1M). In the subsequent experiments, we aimed to determine the effectiveness of CoNZ in the wound healing of acute and chronic inflammatory skin.

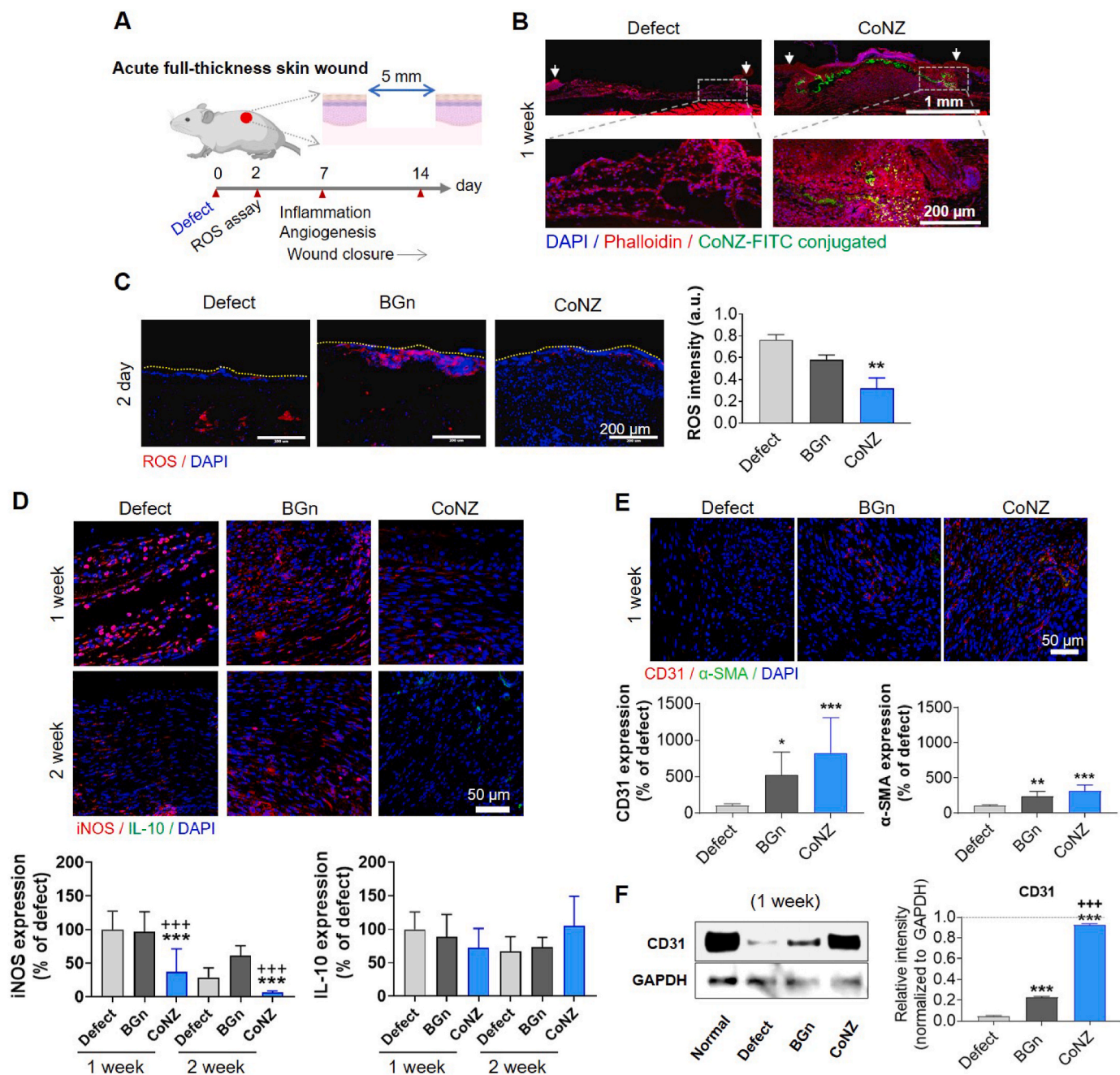


**Fig. 2.** CoNZ effects on anti-inflammation and pro-angiogenesis in full-thickness skin wound. (A) Illustration depicting the *in vivo* full-thickness skin wound model and experimental assays. (B) *In vivo* visualization of administered nanoparticles (CoNZ) by FITC-conjugation; at week 1, FITC-CoNZ nanoparticles were observed distributed within the wound area. (C) ROS signals (in red) in tissue samples at day 2 measured by dihydroethidium dye staining, along with semi-quantitative data using ImageJ; the intense ROS signal within the wound area was significantly reduced in the CoNZ group. (D) Immunohistochemical staining of tissue samples for iNOS (pro-inflammatory signal) and IL-10 (anti-inflammatory signal) at weeks 1 and 2, along with semi-quantitative data using ImageJ; iNOS was down-regulated while IL-10 was up-regulated in the CoNZ group. (E) Immunohistochemical staining of tissue samples for CD31 and  $\alpha$ -SMA (neovascularization) at week 1, along with semi-quantitative data using ImageJ; both signals were expressed at significantly higher levels in the CoNZ group. (F) Western blot analysis of tissue samples for CD31, showing significant differences between groups (defect control < BGn < CoNZ ~ normal tissue); the dotted line (intensity level '1') represents the normal group. Statistical significance was calculated between groups using one-way ANOVA with \* $p < 0.05$ , \*\* $p < 0.01$ , and \*\*\* $p < 0.001$  denoting significance compared to the defect group; and + $p < 0.05$ , +++ $p < 0.001$  indicating significance compared to the BGn group. All data are presented as mean  $\pm$  one standard deviation and the sample size was  $n = 4$ .

2.2. CoNZ accelerates healing events in a full-thickness skin wound

To evaluate the *in vivo* efficacy of CoNZ in wound healing, we generated full-thickness skin wounds in mice (as depicted in supplementary data, Fig. S9). Subsequently, we topically administered 10  $\mu$ L of nanoparticles (BGn or CoNZ) diluted in PBS (10 mg/100  $\mu$ L) at the wound site using a micropipette. The expressions of inflammatory and angiogenic markers were assessed at various time points (Fig. 2A). At week 1, the CoNZ-treated wounds showed distinct fluorescence signals upon FITC conjugation with the nanoparticles (Fig. 2B). As an early indicator of acute injury, we quantified the expression of ROS on day 2 using dihydroethidium dye. We observed high ROS levels (in red) within the wound area, which were significantly reduced in the CoNZ group

(Fig. 2C). Furthermore, we performed immunohistochemical staining of tissue samples for iNOS (pro-inflammatory signal) and IL-10 (anti-inflammatory signal) at weeks 1 and 2. Our results revealed a significant down-regulation of iNOS and up-regulation of IL-10 in the CoNZ group compared to the defect control group, while BGn-treated wounds displayed intermediate expressions (Fig. 2D). In addition, we analyzed neovascularization markers (CD31 and  $\alpha$ -SMA) by immunohistochemical staining of samples at week 1. We found that both markers were expressed at significantly higher levels in the CoNZ group compared to the defect control group (Fig. 2E, and supplementary data Fig. S10) [35]. Furthermore, western blot analysis of tissue samples for CD31 confirmed the IHC data, showing significant differences between sample groups (defect control < BGn < CoNZ ~ normal tissue) (Fig. 2F).

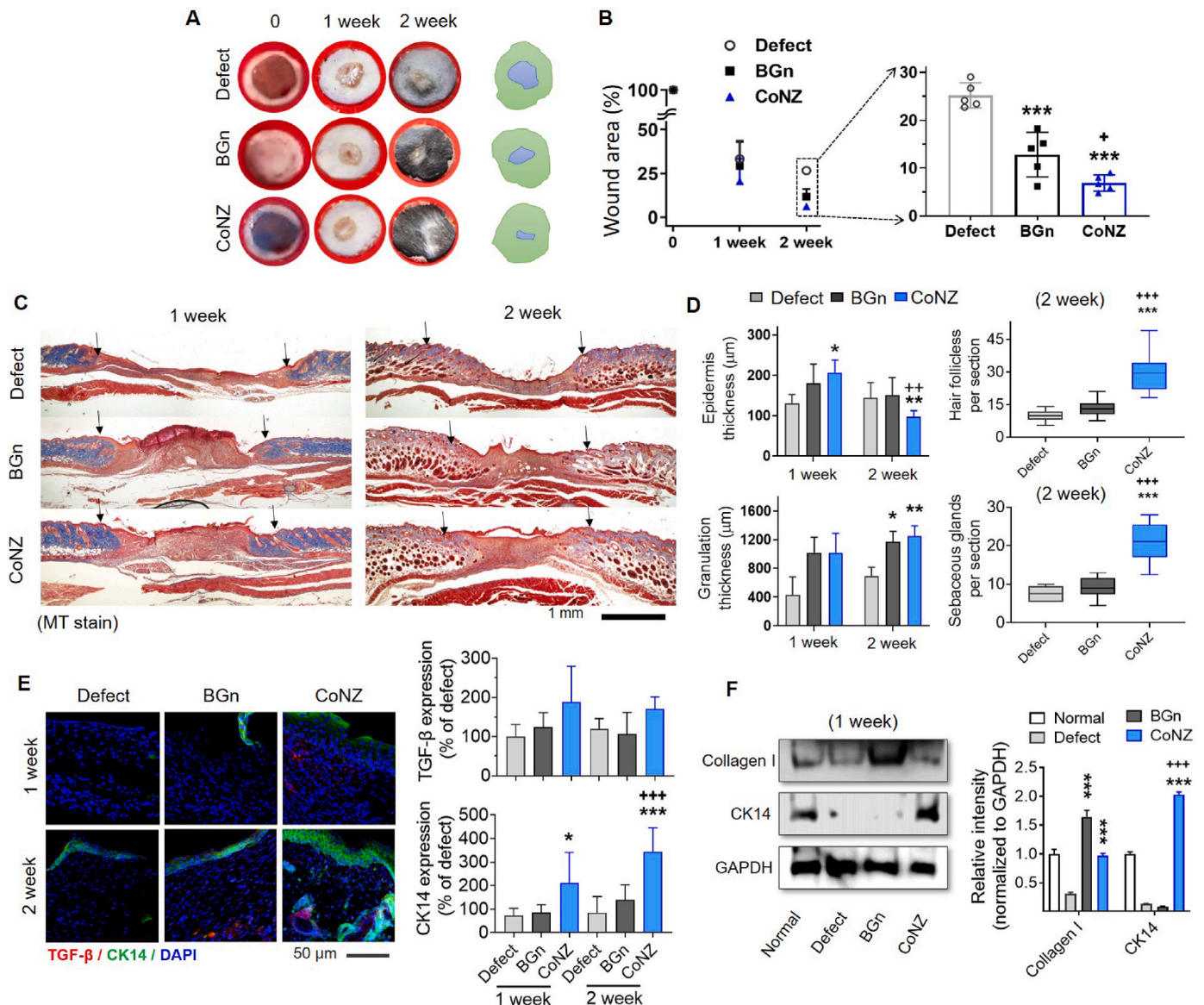


Fig. 3. CoNZ-accelerated healing of full-thickness skin wound with increased matrix synthesis. (A, B) Monitoring of wound closure over 2 weeks; gloss images of defect areas in panel (A) show substantial wound closure over time, and representative wound closure status is also illustrated; wound area was measured in (B), and the data at week 2 were enlarged to show significant differences between groups (wound area remained 5.5% in CoNZ, 11.6% in BGn, and 26.6% in the defect group). (C, D) Masson’s Trichrome (MT) staining images of tissue samples at weeks 1 and 2 demonstrate the regeneration of skin tissue, with the formation of epidermal layer, granulation tissue, hair follicles, and sebaceous glands, along with semi-quantitative data using ImageJ. (E) Immunohistochemical staining of tissue samples for TGF- $\beta$  and cytokeratin 14 (CK14), along with semi-quantitative data using ImageJ. (F) Western blot analysis of tissue samples for type I collagen and CK14, along with semi-quantitative data using ImageJ. Statistical significance was calculated between groups using one-way ANOVA with \* $p$  < 0.05, \*\* $p$  < 0.01, and \*\*\* $p$  < 0.001 denoting significance compared to the defect group; and + $p$  < 0.05, ++ $p$  < 0.01, and +++ $p$  < 0.001 indicating significance compared to the BGn group. All data are presented as mean  $\pm$  one standard deviation and the sample size was  $n = 4$ .

Subsequently, wound closure was monitored at week 1 and 2. The gross images of the wound area demonstrated substantial closure over time (Fig. 3A). Quantitative analysis of wound area (Fig. 3B) showed significant differences between groups, particularly at week 2, where the wound area was 5.5% in CoNZ, 11.6% in BGn, and 26.6% in the defect group. Hematoxylin & Eosin (H&E) and Masson's Trichrome (MT) staining of tissue samples showed regenerated signs of skin tissue with the formation of the epidermal layer and granulation tissue (Fig. 3C & supplementary data in Fig. S11). At week 1, the epidermal layer was almost bridged in the BGn and CoNZ groups, but was only partially formed in the defect group. Over time, from week 1–2, the immature epidermis layer matured, with thickness decreasing particularly in the CoNZ group (Fig. 3D). The tissue granulation was significantly higher in the CoNZ and BGn groups at week 1, which was sustained at week 2 (Fig. 3D), indicating substantial matrix deposition over the period. Of note, the formation of hair follicles and sebaceous glands were measured to be significantly higher in CoNZ group at week 2. The tissue samples were immunohistochemically stained for transforming growth factor- $\beta$  (TGF- $\beta$ ) and cytokeratin 14 (CK14), which are essential markers of fibroblasts and epithelial cells, respectively, particularly for those actively synthesizing ECM (Fig. 3E). Both TGF- $\beta$  and CK14 were expressed at significantly higher levels in the CoNZ group. The western blot analysis of tissue samples further revealed that the expression of type I collagen and CK14 was substantially higher in the CoNZ group (Fig. 3F).

Collectively, our findings demonstrate that the administration of CoNZ to full-thickness acute wounds in mouse skin effectively enhances

wound healing events, such as neovascularization, matrix deposition, and epithelial lining, over a period of two weeks. This was possible by the significantly decreased ROS level and pro-inflammatory responses. Next we examined the efficacy of CoNZ in a more challenging wound condition, namely diabetic wounds, where inflammation is prevalent and neovascularization is significantly limited [42–44].

### 2.3. CoNZ administered to diabetic skin wound reduces inflammation while stimulating angiogenesis and matrix synthesis

To assess the efficacy of CoNZ in a challenging wounding condition, we employed a streptozotocin (STZ) treatment in mice to model diabetic skin wounds (as depicted in Fig. 4A). In this model, wound healing is significantly limited due to severe inflammation and poor neovascularization [45,46]. At day 2, a substantial level of ROS was generated in the defect group, which was significantly reduced by nanoparticle treatment, particularly in the CoNZ-treated group (Fig. 4B). Immunohistochemical staining of pro-inflammatory (iNOS) and anti-inflammatory (IL-10) markers at weeks 1 and 3 (Fig. 4C) revealed that CoNZ treatment significantly reduced iNOS expression while up-regulating IL-10 expression compared to the defect control.

Anti-inflammatory events observed in the *in vivo* diabetic skin wound were further confirmed *in vitro* using macrophages (RAW264.7 cells) exposed to high glucose (HG) to mimic the diabetic *in vivo* environment (experimental design depicted in Fig. 4D). Lipopolysaccharide (LPS) was also administered to upregulate pro-inflammatory ROS in macrophages

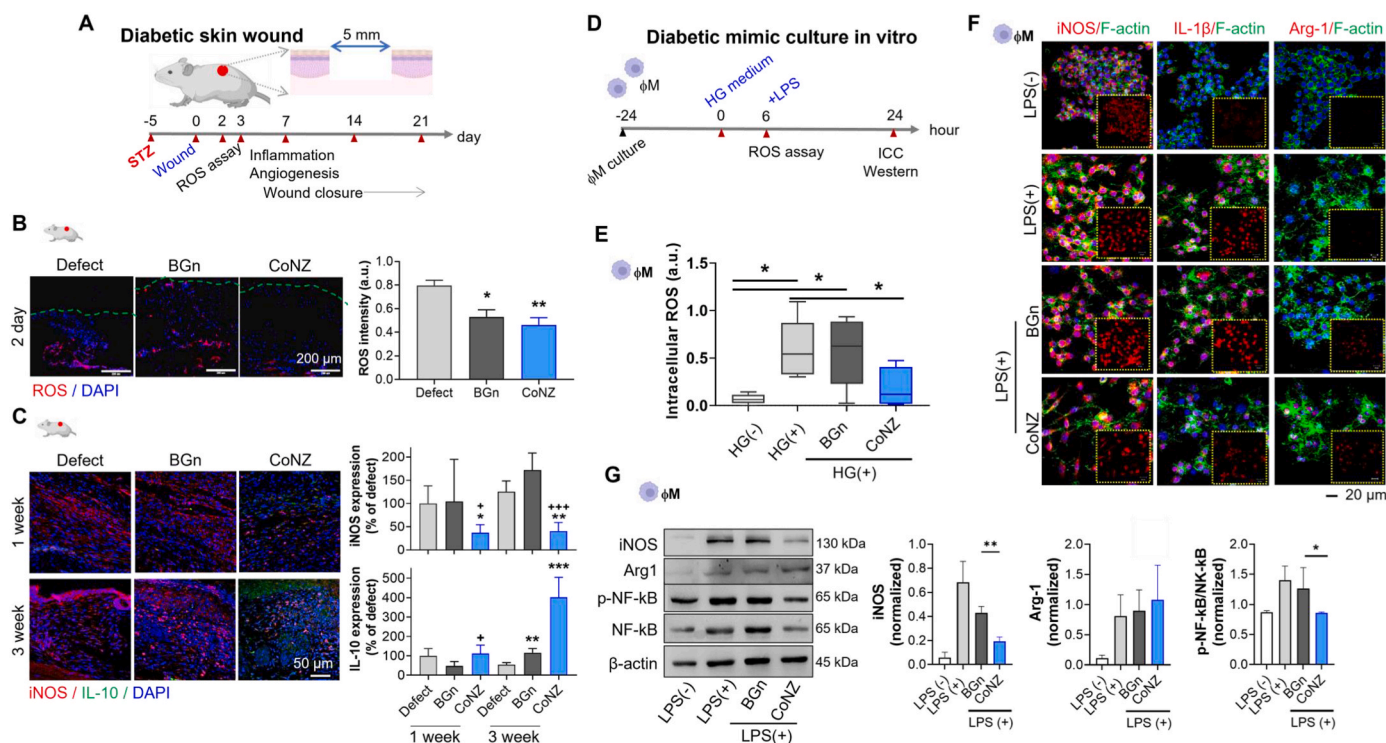


**Fig. 4.** Effects of CoNZ on anti-inflammation *in vivo* and *in vitro*. (A–C) *In vivo* effects of CoNZ in STZ-induced diabetic skin wounds: (A) Illustration depicting the diabetic skin wound model using streptozotocin (STZ) and the assays performed over 21 days. (B) ROS signal (in red) in tissue samples at day 2, and quantification of signal intensity; the intense ROS signal within the defect area was substantially reduced, particularly in the CoNZ group. (C) Immunohistochemical staining of tissue samples for iNOS (pro-inflammatory signal) and IL-10 (anti-inflammatory signal) at week 1 and 3, along with semi-quantitative data using ImageJ; CoNZ down-regulated iNOS but up-regulated IL-10. For the *in vivo* studies, nanoparticles of 10  $\mu$ L from a concentration of 100 mg/1 mL were treated to each wound. (D–G) *In vitro* effects of CoNZ on high glucose- and ROS-challenged inflammatory cells: (D) Diagram of the *in vitro* design that involves macrophages (RAW264.7 cells) challenged with high glucose (HG) and LPS. Nanoparticle concentration used for the *in vitro* study was 20  $\mu$ g/mL. (E) Intracellular ROS signal intensity measured at 6 h. (F) Immunostaining images of cells at 24 h, depicting pro-inflammatory (iNOS, IL-1b) and anti-inflammatory (Arg-1) signals, along with semi-quantitative data using ImageJ. (G) Western blot analysis at 24 h, along with semi-quantitative data using ImageJ, showing iNOS, Arg-1, NF-kB, and its phosphorylated form. Statistical significance was calculated between groups using Unpaired *t*-test and one-way ANOVA with \**p* < 0.05, \*\**p* < 0.01, and \*\*\**p* < 0.001 denoting significance compared to the defect group (*in vivo*) or HG (+)/LPS (-) group (*in vitro*); and +*p* < 0.05, ++*p* < 0.01, and +++*p* < 0.001 indicating significance compared to the BGn group. All data are presented as mean  $\pm$  one standard deviation and the sample size was *n* = 5.

[47–49]. In HG conditions, the macrophages produced significantly higher levels of ROS in HG, which were significantly reduced by CoNZ treatment at 20 µg/mL (Fig. 4E). The cell viability by CCK assay showed a significantly higher level in CoNZ-treated group (by ~1.3-fold increase, supplementary data in Fig. S12A). Immunocytochemical staining at 24 h revealed that CoNZ-treated cells expressed increased anti-inflammatory phenotype (Arg-1) and decreased pro-inflammatory markers (iNOS and IL-1β) (Fig. 4F), indicating macrophage polarization from M1 to M2 phase. Western blot analysis of cells at 24 h revealed substantial down-regulation of iNOS but up-regulation of Arg-1 with CoNZ treatment (Fig. 4G). Additionally, the phosphorylated form of NF-κB, a master regulator of inflammatory cascade reactions in macrophages [50,51], was significantly reduced in the CoNZ-treated group.

Overall, CoNZ administration was effective in reducing pro-inflammatory signs *in vivo*, shifting the status towards less inflammatory in highly inflammable STZ-induced diabetic skin wounds. The *in vivo* findings were further confirmed in *in vitro* experiments involving macrophages exposed to high glucose and ROS generating conditions.

Next, we investigated the impact of CoNZ on angiogenic responses in the diabetic skin wound model. Immunohistochemical staining of neovascularization markers (CD31 and α-SMA) in tissue samples collected at week 1 and 3 showed significantly higher levels in the CoNZ group compared to the defect control group (Fig. 5A). Western blot analysis of tissue samples at week 1 also confirmed the upregulation of CD31 and

HIF-1α in the CoNZ group (Fig. 5B). ELISA analysis of tissue samples revealed that VEGF production was significantly higher in the CoNZ group at day 3, indicating the activation of angiogenic events at an early stage (CoNZ > BGn > defect, in Fig. 5C). VEGF is a master molecule that initiates angiogenic events in endothelial cells [52–55].

To further confirm *in vivo* pro-angiogenic events, we conducted experiments *in vitro* using human umbilical vascular endothelial cells (HUVECs). As illustrated in the experimental design (Fig. 5D), we analyzed the effects of CoNZ on angiogenic events in HUVECs that were challenged with high glucose and H<sub>2</sub>O<sub>2</sub>. In particular, we also added one more group in the comparison (CoNZ-eluted ionic group to decouple the ionic effects from surface-enabled enzymatic/catalytic effects). CoNZ treatment (at 20 µg/mL) significantly reduced the greatly increased intracellular ROS level [10] in HUVECs evoked by high glucose/H<sub>2</sub>O<sub>2</sub> challenge (Fig. 5E). The cell viability by CCK assay showed a slightly higher level in CoNZ-treated group (by ~1.1-fold increase, supplementary data in Fig. S12B). Although the treatment of BGn and CoNZ-ions was only slightly effective, the CoNZ treatment demonstrated notable ROS scavenging abilities (CoNZ ~ CoNZ-ions > BGn > high glucose/H<sub>2</sub>O<sub>2</sub> control). We also examined cell migration over 24 h, as determined by their ability to fill a scratched multicellular gap (Fig. 5F). CoNZ treatment significantly enhanced migration, and interestingly, the treatment of CoNZ-ions was highly effective in cell migration, with levels comparable to the CoNZ treatment. We analyzed the tubular

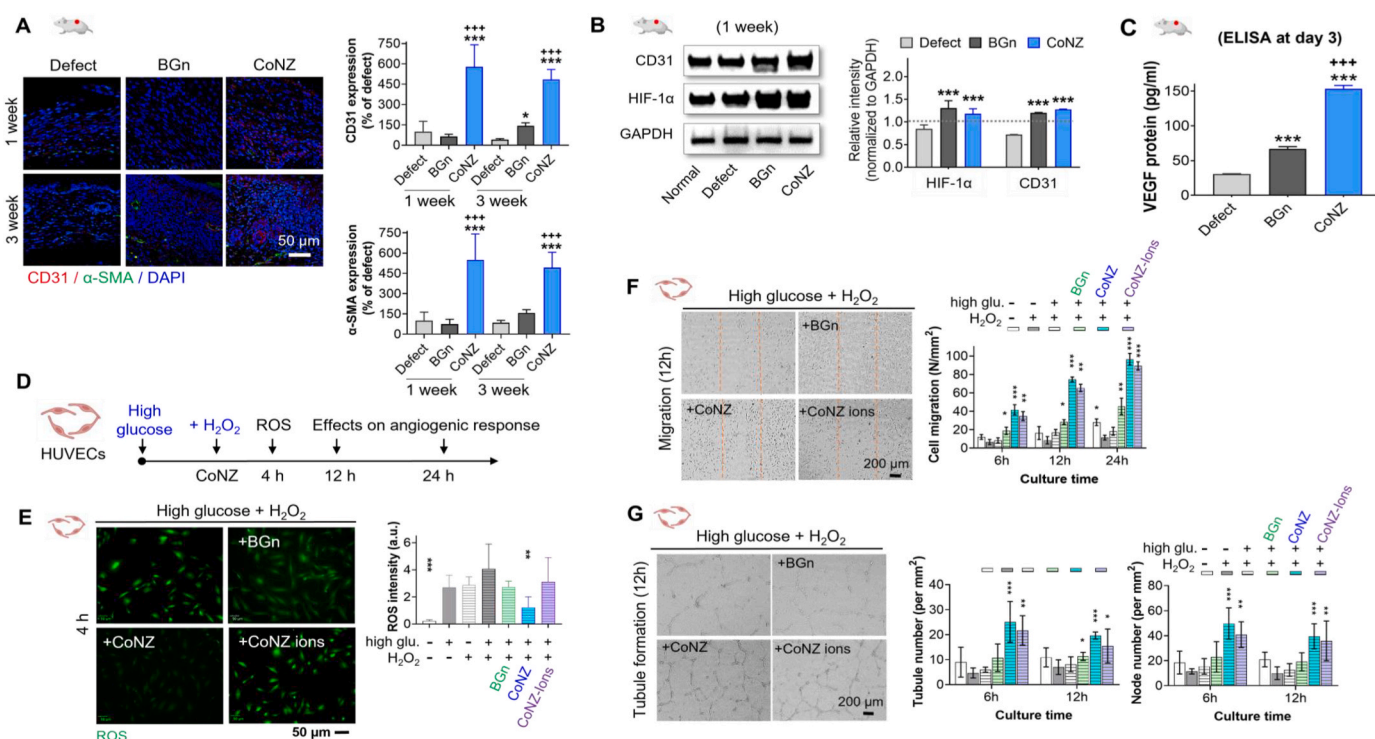


**Fig. 5.** Effects of CoNZ on pro-angiogenesis *in vivo* and *in vitro*. (A–C) *In vivo* experiments with STZ-induced diabetic skin wounds: (A) Immunohistochemical staining of tissue samples for CD31 and α-SMA (neovascularization) at weeks 1 and 3, with semi-quantification of signal intensity by ImageJ; both signals were expressed at significantly higher levels in the CoNZ group. (B) Western blot analysis of tissue samples for CD31 at week 1, showing significant differences between groups (defect control < BGn & CoNZ); the dotted line (intensity level ‘1’) represents the normal group. (C) ELISA analysis of tissue samples for VEGF at day 3. For the *in vivo* studies, nanoparticles of 10 µL from a concentration of 100 mg/1 mL were treated to each wound. (D–G) *In vitro* experiments with high glucose/H<sub>2</sub>O<sub>2</sub>-challenged inflammatory cells. (D) Schematic representation of the *in vitro* design; HUVECs challenged with high glucose and H<sub>2</sub>O<sub>2</sub> were analyzed for angiogenic events. (E) Intracellular ROS level at 12 h; ROS levels substantially increased with high glucose/H<sub>2</sub>O<sub>2</sub> challenge, which were significantly reduced by CoNZ treatment; ROS scavenging ability was observed in the order, CoNZ > CoNZ-ions ~ BGn > high glucose/H<sub>2</sub>O<sub>2</sub> control. Nanoparticle concentration used for the *in vitro* study was 20 µg/mL. (F) Cellular migration was analyzed over 24 h by assessing the ability to fill a scratched multicellular gap; images of four representative groups at 12 h are presented; cell migration was recorded in the order, CoNZ ~ CoNZ-ions > BGn > high glucose/H<sub>2</sub>O<sub>2</sub> control. (G) Tubular formation of cells was examined and quantified in terms of tubule and node number at 6 h and 24 h on a Matrigel substrate; cell images of four representative groups at 24 h are presented. Statistical significance was calculated between groups using one-way ANOVA with \*p < 0.05, \*\*p < 0.01, and \*\*\*p < 0.001 denoting significance compared to the defect group (*in vivo*) or HG (+) & H<sub>2</sub>O<sub>2</sub> (+) group (*in vitro*); and +p < 0.05, ++p < 0.01, and +++p < 0.001 indicating significance compared to the BGn group (*in vivo*). All data are presented as mean ± one standard deviation and the sample size was n = 5.

formation of HUVECs on a Matrigel substrate and observed a significant activation of tubule and node number in the CoNZ group (Fig. 5G). The effect of CoNZ-ions was as high as that of CoNZ. Our *in vitro* results support the effective role of CoNZ in activating neovascularization observed in the *in vivo* diabetic skin wound model. Notably, the significantly stimulated cellular migration and tubular formation (although not as high as in ROS scavenging) in the CoNZ-ions group, which was quite comparable to the CoNZ group, demonstrate the important role of cobalt ions released from the nanoparticles in activating angiogenic events.

As such, the effects of CoNZ in the *in vivo* diabetic skin wound healing, where inflammation prevails while pro-angiogenic events are needed, are explicit; cobalt ionic roles in activating angiogenesis and surface-enabled enzymatic activity of nanoparticles in alleviating pro-inflammatory events. Ultimately these actions shift the chronic wound from a devastating condition towards a reparative phase.

Next, we analyzed the tissue samples at week 1 and 3 by means of H&E and MT staining (Fig. 6A & supplementary data in Fig. S13). The groups treated with nanoparticles, particularly CoNZ, showed significant levels of tissue healing, evidenced by the formation of epidermis layer and granulation tissue, which were limited in the diabetic wound control (Fig. 6A and B). Of note was the generation of hair follicles and sebaceous glands at week 3 in the CoNZ group (enlarged image shown in Fig. 6A). In comparison to normal wound healing, in which the defect control induced some level of healing (e.g., partially formed epidermis

layer), the diabetic wound exhibited limited healing without CoNZ treatment. Administration of nanoparticles was found to be effective in facilitating wound healing, leading to the maturation of thick and immature epidermis layer and granulation tissue towards normal tissue over the healing period of 3 weeks. The significantly higher expression of TGF- $\beta$  and CK14 in the CoNZ group indicates the active events of extracellular matrix (ECM) formation by cells, i.e., TGF- $\beta$  secretion by fibroblasts in the dermis and CK14 by epithelial cells in the epidermis (Fig. 6C). Western blot analysis of tissue samples further confirmed significantly higher expression of ECM molecules (type I collagen and CK14) in the CoNZ group (Fig. 6D).

Collectively, the treatment of CoNZ to STZ-induced diabetic skin wound was found to be highly effective in a series of wound healing events, including the reduction of ROS level and inflammation, the activation of angiogenesis, and the promotion of ECM production.

#### 2.4. Efficacy of CoNZ in diabetic skin wound healing by comparison with commercial drug

Having established the efficacy of CoNZ in accelerating the healing of diabetic skin wounds, we sought to compare its effectiveness with that of a commercial drug. Deferoxamine (DFO) is currently used clinically to treat diabetic ulcers and has been reported to be effective in healing diabetic skin wounds [42,56]. We administered DFO directly to the wound area (100  $\mu$ L at 0.5  $\mu$ M, a known optimal dose), which was

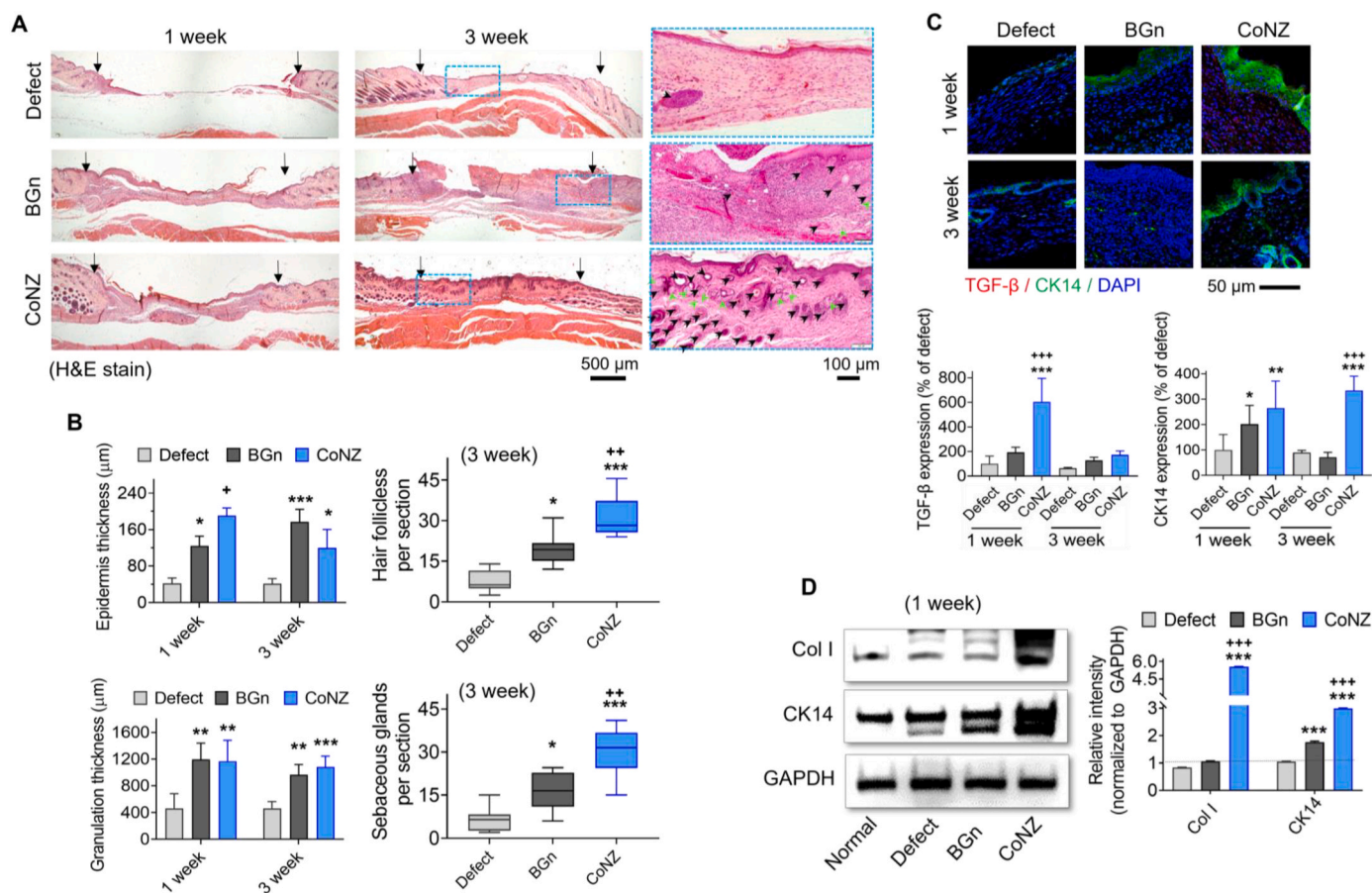


**Fig. 6.** Effects of CoNZ on tissue formation and ECM synthesis in STZ-induced diabetic skin wound. (A) H&E staining of tissue samples at week 1 and 3. In particular, the images (brackets) at week 3 were enlarged to reveal the formation of hair follicles (black arrows) and sebaceous glands (green arrowheads). (B) Analysis of epidermis layer and granulation tissue formation. (C) Immunohistochemical staining of tissue samples for TGF- $\beta$  and CK14, and the semi-quantitative data by ImageJ analysis. (D) Western blot analysis of tissue samples for type I collagen and CK14, and the semi-quantitative data by ImageJ analysis. Statistical significance was calculated between groups using one-way ANOVA with \* $p < 0.05$ , \*\* $p < 0.01$ , and \*\*\* $p < 0.001$  denoting significance compared to the defect group (*in vivo*); and + $p < 0.05$ , ++ $p < 0.01$ , and +++ $p < 0.001$  indicating significance compared to the BGn group. All data are presented as mean  $\pm$  one standard deviation and the sample size was  $n = 8$ .

multiple-dosed every 3 days since a single dose was found to be ineffective in a pilot study. In contrast, the nanoparticle groups (BGn and CoNZ) were locally administered only once (Fig. 7A). We tested a larger number of animals ( $n = 8$  per group) for a more accurate comparison. We monitored the closure of the 5 mm diabetic skin wound over a period of 3 weeks. Results showed that the CoNZ group reduced the wound area more rapidly and effectively than the other groups (significance difference noticed as early as day 3) (Fig. 7B and C). The wound closure of the DFO group was also found to be effective and was intermediate between the CoNZ and BGn groups (CoNZ > DFO drug > BGn > Defect). The quantitative data were further analyzed at two representative time points (day 7 and 21), which clearly demonstrated the significant differences between the groups. These results are noteworthy considering that the CoNZ were administered only once, whereas DFO was dosed multiple times (7 times for 21 days). The hair follicles and sebaceous glands were observed to be well generated in both CoNZ and DFO groups at day 21, with particularly more increased sebaceous glands in CoNZ (Fig. 7D). Since the CoNZ remained in the wound area for at least several weeks (as indicated by the high FITC signal intensity of the FITC-conjugated nanoparticles in the wound area), their biological roles, such as ROS scavenging and anti-inflammatory effects via enzymatic reactions, and angiogenic stimulation by the slowly releasing cobalt (and silicate) ions, are expected to persist during the healing period.

### 3. Summary and outlook

Fig. 8 summarizes the current study, illustrating the dual actions of CoNZ and the underlying molecular mechanisms in the healing events of pathological (diabetic) skin wounds. In this study, we synthesized CoNZ, a bioactive nanozyme with enzymatic and catalytic properties, as well as therapeutic ion release capability. Our findings demonstrated that CoNZ possesses excellent enzymatic activity that scavenges ROS, under high oxidative-stress conditions. This was proven to be highly effective in

both pathological and normal healing processes of wounded skin. The enzymatic and catalytic properties of CoNZ were confirmed by its SOD, peroxidase, and catalase properties, as well as its oxygen generation capacity. Of note, this was reasoned to be due to the presence of “Co<sub>3</sub>O<sub>4</sub>” tiny crystallites distributed in the CoNZ nanoparticles, which is believed to form *in situ* through the chemical reaction with H<sub>2</sub>O<sub>2</sub>, ultimately playing a key role in scavenging various ROS. This distinctive property exhibited by Co<sub>3</sub>O<sub>4</sub> crystallites represents a novel finding with potential implications for mitigating inflammatory-driven diabetic conditions, while the effects of Co-doped bioactive glass on wound healing have been previously documented in other studies [32–35].

The wound healing efficacy of the novel CoNZ was first proven with full-thickness acute wounds in mouse skin, including neo-vascularization, matrix deposition, and epithelial lining. CoNZ treatment was accompanied by significantly decreased ROS level and pro-inflammatory responses. Additionally, we demonstrated the efficacy of CoNZ in the pathological healing process in STZ-induced diabetic skin wound model. Notably, CoNZ treatment led to dramatic healing events that rarely occur naturally, mainly due to the high inflammatory environment that evokes excessive oxidative stress, requiring rapid clearance of ROS and recapitulating resolution environment for surrounding cells (fibroblasts or endothelial cells) to engage in the repair process, such as matrix deposition and angiogenesis. These events were proven by the suppressed ROS level, down-regulated pro-inflammatory molecules, and up-regulated tissue healing signs of proliferative cells and activated angiogenic factors. In particular, the promoted angiogenesis by CoNZ treatment was primarily due to the release of cobalt ions, which was proven by the effects of CoNZ-extracted ionic medium being comparable to those with CoNZ treatment. Released cobalt ions were shown to promote angiogenic functions of cells, including cell migration and tubule formation, by activating HIF-1 $\alpha$  and other angiogenic genes. We further confirmed our *in vivo* findings through *in vitro* experiments involving macrophages and HUVECs exposed to high glucose and ROS-generating conditions.

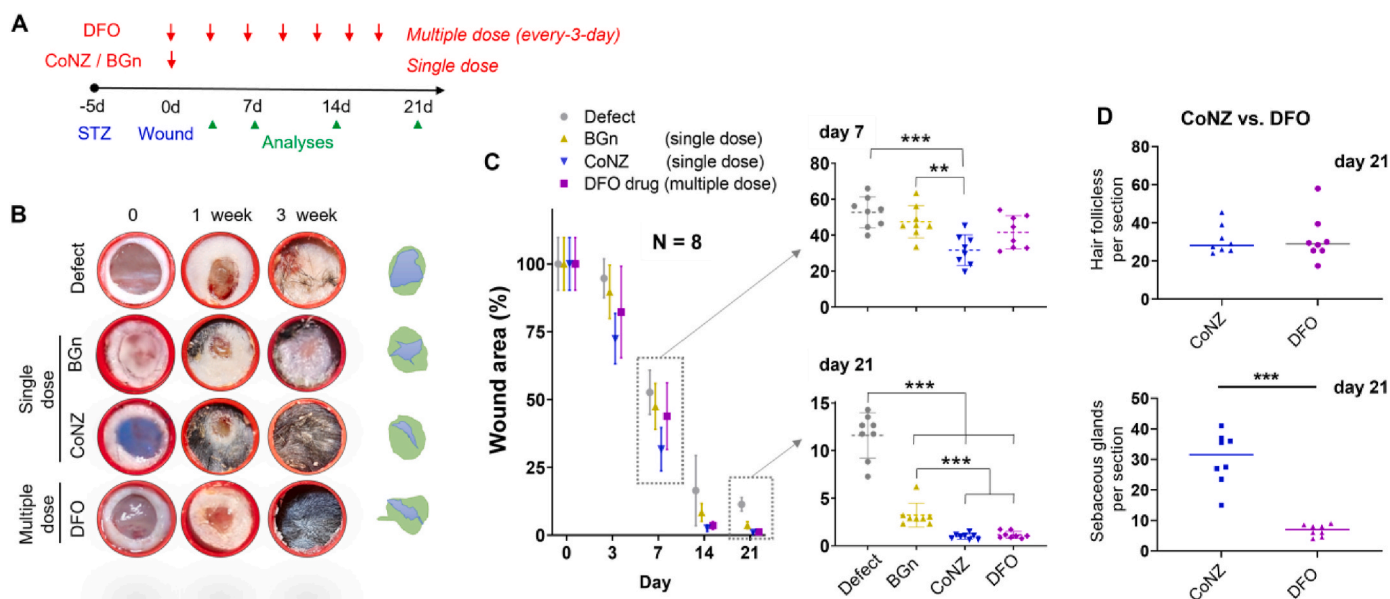


**Fig. 7.** Comparison of diabetic wound healing between CoNZ and commercial drug, deferoxamine (DFO). (A) *In vivo* comparison experiment was designed, wherein DFO was locally administered to the STZ-induced diabetic wound area (100  $\mu$ L at 0.5  $\mu$ M, and multiple-dosed every 3 days), while the nanoparticle groups (BGn and CoNZ) were locally administered only once; a larger number of animals ( $n = 8$  for each group) were used for accurate comparison. (B) Wound closure was monitored over a period of 3 weeks, and representative images are shown. (C) Quantitative analysis of wound areas revealed that the CoNZ group reduced the wound area more rapidly and significantly compared to other groups, with a significant difference observed as early as day 3; DFO drug group also showed effective wound closure, which was in between the CoNZ and BGn groups (CoNZ > DFO drug > BGn > Defect). The quantitative data were enlarged at two representative time points (day 7 and 21). (D) Neo-formation of hair follicles and sebaceous glands was compared between CoNZ and DFO drug groups, showing significantly increased sebaceous glands in CoNZ. Significant differences were noted between groups (one-way ANOVA with \*\* $p < 0.01$  and \*\*\* $p < 0.001$ ).

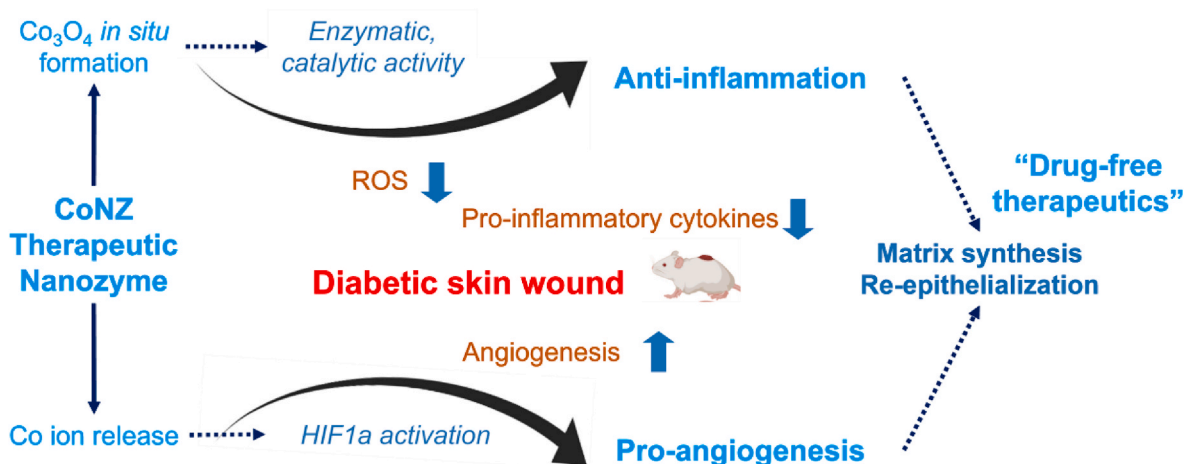


**Fig. 8.** Illustration summarizes current study of the dual functions of CoNZ (anti-inflammatory and pro-angiogenesis) and the underlying molecular mechanisms in the healing events of pathological skin wounds, implying drug-free therapeutics.

Our comparison study with drug deferoxamine (DFO), currently used to treat diabetic ulcers, revealed an effect as high as the drug in closing the wounded area, implying a novel drug-free therapeutic approach. Although further in-depth examination with large animal models is needed, the results are noteworthy as CoNZ was administered only once, compared to the multiple-dosed DFO. Moreover, when the CoNZ nanoparticulate form is combined with wound dressings or injectable gels, there is potential for the treatment of large volumetric diabetic ulcers, which warrants further research.

#### 4. Experimental section

##### 4.1. Synthesis and characterizations

Nanoparticles based on the bioactive nanoglass composition, 15% CaO - 85% SiO<sub>2</sub> (wt%), were synthesized using a base-catalyzed sol-gel route employing polyethylene glycol (PEG) as a structure-directing template, as described in our previous works [57–59]. CoO was added to the nanoglass composition in replacement of CaO, with a chemical formula of x% CoO - (15-x) % CaO - 85% SiO<sub>2</sub> (wt %), where x = 1, 2.5, 5, and 10%. Briefly, calcium nitrate tetrahydrate and the corresponding amount of cobalt (II) nitrate hexahydrate were solubilized in PEG solution (5g, 120 mL ethanol/30 mL ammonia). Tetraethoxysilane solution (0.95 mL/30 mL ethanol) was then added dropwise under vigorous stirring and ultrasound irradiation. Ultrasound irradiation (10 Sec on/off) was stopped after 20 min while stirring was continued for 24 h. The precipitates were separated and washed several times. The collected precipitates were dried in an oven at 70 °C overnight. Finally, the dried precipitates were heat-treated at 600 °C under air flow for 5 h. The final products were stored under vacuum for further uses.

X-ray diffraction (XRD) was utilized to ensure the glass phase of the nanoparticles. X-ray (CuK<sub>α</sub> radiation, λ = 1.5418 Å) was generated at 40 kV and 40 mA using Rigaku-Ultima IV (Japan). Surface charge was examined by ζ-potential measurement (Zetasizer Nano ZS, Malvern, UK). The ζ-potential was measured in a deionized water (pH 7.4) at 25 °C with applied field strength (20 V/cm). Five measurements (an average of 40 runs) were performed.

The nanoscale morphology was examined by high-resolution transmission electron microscopy (HR-TEM, JEM-ARM200F, Cold FEG, JEOL Ltd, Japan). The size of nanoparticles was measured based on the HR-TEM images (n = 77 particles, arbitrarily chosen) and then analyzed with Digimizer image analysis software (MedCalc software, Belgium). The textural properties, including specific surface area, pore size, and pore volume, were determined by N<sub>2</sub>-sorption using the Quantachrome instrument (Quadrasorb SI, USA) after degassing the sample at 300 °C

overnight. The specific surface area was measured using the Brunauer-Emmett-Teller (BET) method, while pore size and pore volume were analyzed using Non-Local Density Functional Theory (NLDFT). A complete survey and high-resolution X-ray photoelectron spectroscopy (XPS, K-alpha, Thermo VG, U.K.) were performed using the Al K<sub>α</sub> line (1486.6 eV) as the X-ray source.

The release of ions (including cobalt, calcium, and silicate) was examined by inductively coupled plasma atomic emission spectrometry (ICP-AES, Optima 4300DV, Perkin-Elmer). Samples were immersed in Tris-HCl buffer (50 mg/10 mL) at physiological conditions (37 °C, pH 7.4) with shaking at 120 rpm. Three replicate samples were analyzed.

##### 4.2. Analyses of enzymatic and catalytic activity

The peroxidase mimetic activity of nanoparticles was evaluated by monitoring the redox reaction between 3,3',5,5'-tetramethylbenzidine (TMB) and hydrogen peroxide (H<sub>2</sub>O<sub>2</sub>) in the presence of the nanoparticles. Upon peroxidation, TMB is oxidized into its oxTMB form, producing a blue color in the solution. Briefly, a 96-well plate containing 200 μl of acetate-acetic acid buffer solution (200 mM, pH = 4.0), 20 μg of nanoparticle solution (1 mg/mL), 0.5 μmol of TMB, and 1 mmol of H<sub>2</sub>O<sub>2</sub> was used in the experiment. The reaction was monitored using a multi-detection microplate reader (SpectraMaxM2e, Molecular Devices Corporation, San Jose, USA) at a wavelength of 652 nm. The measurement was recorded after 1 min, and the temperature was maintained at 37 °C.

The superoxide dismutase mimetic activity was evaluated using the OxiSelect™ Superoxide Dismutase Activity Assay kit (CELL BIOLABS, USA) based on a colorimetric method. This assay kit generates superoxide anions (O<sub>2</sub><sup>-</sup>) using a Xanthine/Xanthine oxidase (XOD) system, which are then detected with a chromogenic solution containing the formazan dye. In the presence of SOD, the concentration of these superoxide anions is reduced, resulting in a reduced colorimetric signal. The experimental protocol was followed precisely, except that 10 μg of the sample was used in the assay.

The catalase mimetic activity of NPs was evaluated by monitoring the production of oxygen. Since we did not have a sensor to measure the dissolved oxygen concentration, we indirectly observed the production rate of oxygen as previously reported in Ref. [47]. Briefly, the catalase mimetic activity of nanoparticles was evaluated by monitoring the absorbance of the H<sub>2</sub>O<sub>2</sub> solution. Well-dispersed nanoparticles were immersed into diluted H<sub>2</sub>O<sub>2</sub> solution and incubated in a 37°C oven for 1 h. Then, the remaining concentration of the H<sub>2</sub>O<sub>2</sub> solution was measured at 240 nm after removing the nanoparticles by centrifugation at 15,000 rpm.

#### 4.3. Electrochemical assay: oxygen reduction and evolution reaction

The redox properties of nanoparticles in solution are closely related to their enzymatic properties. To investigate their catalytic activity in oxygen reduction reaction (ORR) and oxygen evolution reaction (OER), cyclic voltammetry was performed in 0.1 M KOH solution. A slurry was prepared by mixing 2 mg of catalyst powder, 4 mg of Vulcan carbon (an electron conductor), 1 mL of isopropyl alcohol (IPA), and 70  $\mu$ l of Nafion 520 solution (a binder). A drop of the well-mixed solution (6  $\mu$ l) was coated on a glassy carbon electrode (catalyst loading = 34  $\mu$ g and geometric area = 0.2 cm<sup>2</sup>) and set up using a three-electrode system from Pine Instruments, with a rotating electrode assembly. A 1 M NaOH Hg/HgO reference electrode (0.14V vs. RHE) and a platinum wire counter electrode were used. Linear sweep voltammetry (LSV) was performed for ORR and OER at a range of 0.05–1.23 V or  $V_{RHE}$  and 1.2–2.0  $V_{RHE}$ , respectively, with a scan rate of 20 mV/s in an oxygen-saturated atmosphere at 1600 rpm.

#### 4.4. FITC conjugation of nanoparticles

To conjugate fluorescein isothiocyanate (FITC) with the nanoparticles, 0.0357 g (0.0917 mmol) of FITC (Sigma, isomer I) was dissolved in 0.1827 g (0.8252 mmol) of vacuum-distilled 3-(amino-propyl)-triethoxylane (Sigma). The mixture was stirred for 24 h in the dark. The amino group of the silane coupling agent APS reacted with the isothiocyanate group of FITC to form N-1-(3-triethoxylpropyl)-N'-fluoresceyl-thiourea. The resulting slurry was dissolved in 1.3 mL of anhydrous ethanol, producing a clear solution called APS-FITC. For surface labeling of CoNZ, 0.1 mg of APS-FITC was added to 1 mg/mL CoNZ ethanol solution. The reaction was stirred for 16 h at room temperature in the dark, and the resulting products were recovered by centrifugation. CoNZ-FITC was washed with ethanol and DW to remove unbound FITC and then dried by freeze-drying for 24 h.

#### 4.5. Cells and culture media

Two different culture media were prepared to mimic normal and high glucose conditions. The normal glucose media contained 5.5 mM D-glucose, which is a reasonable glucose concentration found in the body and is commonly used in cell proliferation media. The high glucose media contained 30 mM D-glucose, which mimics hyperglycemia, a diabetic blood glucose level (supplementary data in Table S3).

Human Umbilical Vein Endothelial cells (HUVEC) and media were purchased from ATCC and cultured following the manufacturer's guidelines. The RAW 264.7 cell line was also cultured according to general protocols. The cells were seeded at a density of 10<sup>4</sup> RAW 264.7 and 6 × 10<sup>3</sup> HUVEC cells per well in 96-well plates and treated with different concentrations (0–320  $\mu$ g/mL) of nanoparticles in normal and high glucose media. The cell counting assay (CCK-8 kit, Dojindo Laboratories, Japan) was used to estimate viable cell number, and all analyses were performed in triplicate.

#### 4.6. Endothelial migration and tubule formation

HUVECs were cultured in 24-well plates with a Culture-Insert 2 well (Cat #80209, ibidi®, Germany) according to the manufacturer's instructions at a density of 3 × 10<sup>5</sup> cells/mL. The cells were then incubated overnight in media containing 10  $\mu$ g/mL of Mitomycin C (M4286, Sigma Aldrich) for 1 h to suppress cell proliferation. A 500  $\mu$ m scratch wound was created in the confluent monolayer using a Culture-Insert 2 well ring, which was removed afterwards. The cells were gently rinsed with Hank's Balanced Salt Solution (HBSS), and the wounded monolayers were cultured in 2% FBS low glucose (5 mM D-glucose) and high glucose (30 mM D-glucose) medium. Prior to treatment with ionic dissolution products prepared in the high glucose medium under H<sub>2</sub>O<sub>2</sub> (200  $\mu$ M) condition, the cells were pre-treated with nanoparticles (20  $\mu$ g/mL).

To evaluate *in vitro* tubular formation, we conducted an assay using matrigel (BD Bioscience, Europe). Following the manufacturer's instructions, approximately 300  $\mu$ l/well of Matrigel was coated in 24-well plates, and then 10<sup>4</sup> cells were seeded and treated with materials under H<sub>2</sub>O<sub>2</sub> conditions. The cells were observed at each time point (0, 3, 6, and 12 h) using an inverted light microscope (IX-71; Olympus, Japan). Mesh-like circles (circle), number of branch points (nodes), and the total length and size of the formed tubules were measured in ImageJ, as previously described [41,60].

#### 4.7. In vitro intracellular ROS assay

To evaluate intracellular ROS levels *in vitro*, we used the c-H<sub>2</sub>DCFDA probe from the Image-iT Live Green ROS kit (Thermo Fisher). Before ROS measurement, cells were cultured in proliferation media overnight. After incubation, nanozymes (20  $\mu$ g/ml) were added to the cells and treated with media containing two different glucose levels (LG and HG) for 6 h. Afterwards, the cells were treated with H<sub>2</sub>O<sub>2</sub> (200  $\mu$ M) for 20 min. Following the manufacturer's protocol, the ROS assay used 10 mM c-H<sub>2</sub>DCFDA to estimate ROS expression, indicated by green fluorescence. The nucleus was stained with Hoechst (blue). The fluorescence signal intensity was quantified by ImageJ software.

#### 4.8. Immunofluorescence assay

The RAW 264.7 cells were first treated with nanoparticles (20  $\mu$ g/mL), followed by stimulation with LPS (100 ng/mL) under high glucose conditions for 24 h (for ICC and WB analysis). Subsequently, immunocytochemistry staining was performed using a general protocol. Briefly, the cells were fixed in 4% paraformaldehyde (PFA), permeabilized with Triton X-100, and blocked with a commercially available solution (DAKO). Dilutions of primary antibodies (supplementary data in Table S2) were prepared using 3% bovine serum albumin (BSA) (Sigma) in 0.1% Tween-phosphate-buffered saline (TPBS). For macrophage staining, primary antibodies against iNOS (1:100, rabbit, PA1-036, Thermo Fisher), IL-1b (1:100, rabbit, P420B, Thermo Fisher), and Arg-1 (1:200, rabbit, PA5-29645, Thermo Fisher) were treated overnight at 4 °C. After three washing steps, secondary antibodies, including F-actin (Alexa Fluor™ 488, Invitrogen), Rhodamine, and FITC conjugated (1:200, Jackson Immuno Research, Inc.), were treated for 1 h at room temperature (RT). DAPI was used for counterstaining. The IF staining sections were analyzed using a confocal laser scanning microscope (CLSM; Zeiss LSM 700 and IX71, Olympus), and the quantitative analysis was performed using ImageJ software.

#### 4.9. Animal model: full-thickness skin wound healing

*In vivo* experiments were conducted to study skin wound healing using a mouse model. The protocol followed was based on previous studies and aimed to promote cutaneous regeneration and prevent wound contraction by splinting silicone rings. All surgical procedures were performed in accordance with the guidelines approved by the Institutional Animal Care and Use Committee at Dankook University (approval no. DKU-18-032), Republic of Korea. A total of eight healthy male C57BL/6 wild-type mice, aged eight weeks, were used in the study. The animals were housed in a specific pathogen-free (SPF) facility with controlled atmosphere and humidity conditions, ad libitum access to water, and food provided. They were exposed to a light/dark cycle and received appropriate care according to the animal care protocol.

The mice were anesthetized using continuous application of isoflurane during the procedures. The dorsal area hair was trimmed to mimic the hair stage of anagen using a cream, washed with a povidone-iodine solution, and cleaned with an alcohol swab. A circular, full-thickness dorsal wound (surface area 19.69 mm<sup>3</sup>) was created on each animal using a 5-mm biopsy punch (Kaj medical, Japan), and doughnut-shaped silicone splints ( $\varnothing$  14 mm x  $\varnothing$  8 mm x h 2 mm) were fixed around

the wound using silicone glue (ELASTOSIL E43, German) and dafilon 4/0 sutures to prevent skin contraction. This created a murine skin wound healing model in which a rubber splint fixed to the wound edges limits the normal wound contraction of rodents, thereby simulating a better native healing response in humans and fixed-skinned mammals. Materials (sham group with only saline and two experimental groups with the treatment of BGn or CoNZ) were applied to the wounds. From a nanoparticle concentration of 100 mg/1 mL, an aliquot of 10  $\mu$ L was applied to each wound. The wound sites were further covered with Tegaderm (3M™) and Coban TM (3M™) bandage to minimize water loss and protect them from animal scratching. Optical images of the wounds were captured at each time point (days 0, 3, 7, 14, and 21) and analyzed using Image J software. Closed wound areas were quantified by the pixel area of the wounds at the designated time points normalized to the pixel area of the initial wound image captured on day 0 for each mouse.

Tissue samples were collected and immediately fixed in 10% neutral buffered formalin under normal conditions. For further analysis, samples were embedded in either OCT or paraffin, sectioned, and stained using standard histological protocols, including H&E, Masson's Trichrome, and immunofluorescence staining.

#### 4.10. Animal model: streptozotocin-induced diabetes mellitus

To induce experimental diabetes mellitus, Streptozotocin (STZ) [61, 62] (Sigma-Aldrich Corp., St. Louis, USA) was used at a dosage of 50 mg/kg, administered intraperitoneally (IP) in ten-week-old male C57BL/6 mice for five consecutive days [63,64]. The STZ was prepared using 0.1 M citrate buffer (pH 4.5), while a control group received 100  $\mu$ L of the same buffer via IP injection. The diabetic state was confirmed by measuring blood glucose levels from tail venous blood using a fast glucometer (Accu-Chek®, Roche, USA) under the inhalation gas (Isoflurane, Hana Pharm Co., Ltd, Korea) one week after STZ treatment. Only mice with a blood glucose concentration over 400 mg/dL were used for the study.

To establish a chronic wound model, these diabetic mice were divided into experimental groups: CoNZ, BGn, medium only, and in particular, 500  $\mu$ M of deferoxamine (DFO) drug was also used for comparison group [42]. DFO was treated every 3 days (at day 0, 3, 6, 9, 12, 15, and 18, thus 7 times in total until 21 days of implantation), whereas CoNZ was treated only once (at day 0). The wound healing was examined in all groups at weeks 1 and 3 post-treatment ( $n = 8$ ). Prior to transplantation, STZ-treated C57BL/6 mice were retested to confirm diabetic state and only mice with non-fasted blood glucose levels exceeding 300 mg/dl were used. Blood glucose levels were monitored throughout the study period, with one blood droplet collected from the tail vein by lancet and tested using the Clarity Plus commercial glucometer.

#### 4.11. In vivo ROS level analysis

As reported previously [10], *in vivo* levels of reactive oxygen species (ROS) in the vicinity of the wound were assessed. Briefly, the initial 2-day period after NZ implantation was analyzed. On day one after injury, each animal was injected with dihydroethidium (DHE; 20 mg/kg, 100  $\mu$ L) via intravenous (IV) injection. Wound tissues were collected, cryo-sectioned to a thickness of 10  $\mu$ m, and counterstained with Hoechst. The red signals were visualized and quantified using a fluorescence microscope and ImageJ software.

#### 4.12. ELISA assay for VEGF determination

Quantikine murine VEGF ELISA kit (MMV00, R&D Systems) was used to detect the VEGF quantity released from HUVECs after culturing for 3 days, following the manufacturer's protocols. In brief, tissue samples were collected using a biopsy punch and subsequently washed with PBS and then homogenized. Following several freezing/thawing

cycles, the samples underwent centrifugation for 5 min and were prepared for the assay. In each well, 50  $\mu$ L of assay diluent RD1N and the sample were added and incubated at room temperature for 2 h. After thorough washing, 100  $\mu$ L of VEGF-conjugate was added to each well and incubated at room temperature for another 2 h. Following additional washing steps, 100  $\mu$ L of substrate solution (diluted in a 1:1 ratio) was incubated at room temperature for 30 min. The reaction was halted by adding the stop solution, and the optical density was measured at 450 nm within 30 min.

#### 4.13. Western blot analysis

To harvest new tissue from the defect area, a 5 mm biopsy was taken and the resulting tissue was measured (10 mg/600  $\mu$ L) before being lysed in ProPrep™ protein extraction solution (iNtRON Biotechnology, 17081). The tissue was then homogenized using a Biomasher® tube until a homogeneous suspension was achieved, and incubated on ice for 20–30 min. The resulting supernatant was collected after centrifugation (13,000 rpm for 5 min, at 4 °C) and stored at –80 °C until subsequent analysis.

Protein content was determined using the Bradford protein assay according to the manufacturer's protocol (BioRad, 500-0201) with reducing agent buffer (Thermo Fisher, B0007 and B0009). Specifically, 20  $\mu$ g of total protein were loaded onto 4–12% slope Bolt Bis-Tris Plus pre-cast gels (Invitrogen, NW04120BOX) and electrophoresed at a constant voltage in MOPS buffer (Invitrogen, B000102). The separated proteins were then transferred to PVDF membranes (iBlot™ 2 Transfer Stacks, PVDF, mini, IB24002) using the iBlot™ 2 Gel transfer device (Thermo Fisher, IB21001). The PVDF membranes were incubated with primary and secondary antibodies using the iBind™ Flex Western device (Invitrogen, SLF2000) and iBind™ Flex Card (Invitrogen SLF2010).

Detection of the immuno-labelled proteins was performed using the enhanced chemiluminescence (Pierce™ ECL Western Blotting Substrate) technique as described by the manufacturer (Thermo Fisher, 32106), and membrane imaging was observed in ImageQuant™ LAS4000 (GE Healthcare Life Science). The optical density of each band was standardized to the corresponding intensity band of GAPDH and quantified (The primary antibodies used are listed in Table S2 of the supplementary data.).

#### 4.14. Morphometric analysis

The wound closure was measured based on optical images and histological analysis. For optical image analysis, wound photographs were taken with a camera at the predicted time points, and the wound areas were measured using ImageJ software. Sectioned samples were stained with H&E and MT for histology quantification. Images were observed with an Olympus inverted microscope (IX71, Olympus). The extent of loading edge ratio ( $\mu$ m) was calculated as the initial length of the wound divided by the length of the epithelial tongues. Re-epithelialization (%), the thickness of granulation tissue ( $\mu$ m), and epithelial thickness ( $\mu$ m) were determined using H&E staining images.

#### 4.15. Immunohistochemistry

Immunohistochemistry staining was used to detect specific proteins in the wound tissues after treatment. The tissue was first treated with an antigen retrieval solution (0.01 M citrate buffer, pH 6, at 95 °C for 10 min) and then blocked with a DAKO blocking solution (Agilent, DAKO). To permeabilize the cell membrane, 0.2% Triton X100 was applied before the primary antibody. The primary antibody dilution was prepared with 3% BSA (Sigma) in 0.1% TPBS, and the primary antibodies used are listed in the supplementary data (Table S2). Macrophage primary antibodies included iNOS (1:100, rabbit, PA1-036, Thermo Fisher), IL-1b (1:100, rabbit, P420B, Thermo Fisher), Arg-1 (1:100, rabbit, PA5-29645, Thermo Fisher), and IL-10 (1:100, rat, ab18939,

abcam); for vessels, CD31 (1:50, rabbit, PA5-16301, Thermo Fisher) and a-SMA (1:50, mouse, sc-53015, Santa Cruz) were used; for regeneration, Cytokeratin-14 (1:100, mouse, ab7800, abcam) and TGF- $\beta$  (1:100, rabbit, 3711S, Cell signalling) were used. The primary antibodies were incubated with the tissue overnight at 4 °C. After washing the tissue sections three times for 5 min each, secondary antibodies conjugated with Rhodamine and FITC (1:200, Jackson Immuno Research, INC) or FITC (Rat, NB7114, Novus) were applied for 1 h at room temperature. DAPI was used for counterstaining. The immunofluorescence staining sections were then analyzed using a confocal laser scanning microscope (CLSM; Zeiss LSM 700 and IX71, Olympus), and the quantitative analysis was performed using ImageJ software.

#### 4.16. Statistical analysis

All experiments were performed in multiple numbers to ensure reproducibility, and statistical analyses were conducted using GraphPad Prism software. The data are presented as means  $\pm$  standard deviation, and statistical significance was assessed using a one-way analysis of variance (ANOVA) followed by Tukey's post hoc test or an unpaired *t*-test, as appropriate. The level of significance was set at  $p < 0.05$ ,  $p < 0.01$ , or  $p < 0.001$ .

#### Ethics approval and consent to participate

All authors declare that we followed all the ethics related with this work. We also confirm that this manuscript, in whole or in part, has not been submitted to any other scientific journal at the time of submission, and all authors agree to the content and being listed as authors on the manuscript.

#### CRedit authorship contribution statement

**Nandin Mandakbayer:** Conceptualization, Data curation, Investigation, Methodology, Visualization, Writing – original draft, Writing – review & editing. **YunSeong Ji:** Conceptualization, Data curation, Formal analysis, Methodology, Writing – original draft. **Ahmed El-Fiqi:** Data curation, Methodology. **Kapil D. Patel:** Data curation, Methodology. **Dong Suk Yoon:** Data curation, Methodology. **Khandmaa Dashnyam:** Data curation, Visualization. **Oyunchimeg Bayaraa:** Data curation, Methodology. **Gangshi Jin:** Data curation, Methodology. **Khaliunsarnai Tsogtbaatar:** Data curation, Visualization. **Tae-Hyun Kim:** Data curation, Methodology. **Jung-Hwan Lee:** Conceptualization, Methodology, Visualization, Writing – original draft. **Hae-Won Kim:** Conceptualization, Supervision, Visualization, Writing – original draft, Writing – review & editing.

#### Declaration of competing interest

HW Kim is an editorial board member for Bioactive Materials and was not involved in the editorial review or the decision to publish this article. All authors declare that there are no competing interests.

#### Acknowledgements

This work was supported by the National Research Foundation of Korea (2021R1A5A2022318, 2018K1A4A3A01064257, 2019R1A6A1A11034536, RS-2023-00220408, 2022K1A3A1A08085419, 2021R1I1A1A01049104).

#### Appendix A. Supplementary data

Supplementary data to this article can be found online at <https://doi.org/10.1016/j.bioactmat.2023.08.014>.

#### References

- [1] J. Quan, Z. Zhao, L. Wang, C.S. Ng, H.H.Y. Kwok, M. Zhang, S. Zhou, J. Ye, X. J. Ong, R. Ma, G.M. Leung, K. Eggleston, M. Zhou, Potential health and economic impact associated with achieving risk factor control in Chinese adults with diabetes: a microsimulation modelling study, *Lancet Reg. Heal. - West. Pacific*. 33 (2023), 100690, <https://doi.org/10.1016/j.lanwpc.2023.100690>.
- [2] R.T. Eberhardt, J.D. Raffetto, Chronic venous insufficiency, *Circulation* 130 (2014) 333–346, <https://doi.org/10.1161/CIRCULATIONAHA.113.006898>.
- [3] G.C. Gurtner, S. Werner, Y. Barrandon, M.T. Longaker, Wound repair and regeneration, *Nature* 453 (2008) 314–321, <https://doi.org/10.1038/nature07039>.
- [4] H. Sies, D.P. Jones, Reactive oxygen species (ROS) as pleiotropic physiological signalling agents, *Nat. Rev. Mol. Cell Biol.* 21 (2020) 363–383, <https://doi.org/10.1038/s41580-020-0230-3>.
- [5] V. Falanga, Wound healing and its impairment in the diabetic foot, *Lancet* 366 (2005) 1736–1743, [https://doi.org/10.1016/S0140-6736\(05\)67700-8](https://doi.org/10.1016/S0140-6736(05)67700-8).
- [6] Y. Guan, H. Niu, Z. Liu, Y. Dang, J. Shen, M. Zayed, L. Ma, J. Guan, Sustained oxygenation accelerates diabetic wound healing by promoting epithelialization and angiogenesis and decreasing inflammation, *Sci. Adv.* 7 (2021) 153–180, <https://doi.org/10.1126/SCIADV.ABJ0153>.
- [7] E. Shaabani, M. Sharifiaghdam, R. Faridi-Majidi, S.C. De Smedt, K. Braeckmans, J. C. Fraire, Gene therapy to enhance angiogenesis in chronic wounds, *Mol. Ther. Nucleic Acids* 29 (2022) 871–899, <https://doi.org/10.1016/j.omtn.2022.08.020>.
- [8] C.G. Wang, Y.T. Lou, M.J. Tong, L.L. Zhang, Z.J. Zhang, Y.Z. Feng, S. Li, H.Z. Xu, C. Mao, Asperosaponin VI promotes angiogenesis and accelerates wound healing in rats via up-regulating HIF-1 $\alpha$ /VEGF signaling, *Acta Pharmacol. Sin.* 39 (2018) 393–404, <https://doi.org/10.1038/aps.2017.161>.
- [9] H. Zhao, J. Huang, Y. Li, X. Lv, H. Zhou, H. Wang, Y. Xu, C. Wang, J. Wang, Z. Liu, ROS-Scavenging Hydrogel to Promote Healing of Bacteria Infected Diabetic Wounds, *Biomaterials*, 2020, 120286, <https://doi.org/10.1016/j.biomaterials.2020.120286>.
- [10] R.K. Singh, D.S. Yoon, N. Mandakbayer, C. Li, A.G. Kurian, N.H. Lee, J.H. Lee, H. W. Kim, Diabetic Bone Regeneration with Nanoceria-Tailored Scaffolds by Recapitulating Cellular Microenvironment: Activating Integrin/TGF- $\beta$  Co-signaling of MSCs while Relieving Oxidative Stress, *Biomaterials*, 2022, <https://doi.org/10.1016/j.biomaterials.2022.121732>.
- [11] F.M. Acosta, K. Stojkova, J. Zhang, E.I. Garcia Huitron, J.X. Jiang, C.R. Rathbone, E.M. Brey, Engineering functional vascularized beige adipose tissue from microvascular fragments of models of healthy and type II diabetes conditions, *J. Tissue Eng.* 13 (2022), <https://doi.org/10.1177/20417314221109337>.
- [12] R. D'Amico, C. Malucelli, A. Uccelli, A. Grosso, N. Di Maggio, P.S. Briquez, J. A. Hubbell, T. Wolff, L. Gürke, E. Mujagic, R. Gianni-Barrera, A. Banfi, Therapeutic arteriogenesis by factor-decorated fibrin matrices promotes wound healing in diabetic mice, *J. Tissue Eng.* 13 (2022), <https://doi.org/10.1177/20417314221119615>.
- [13] T. Serena, R. Yaakov, S. Aslam, R. Aslam, Preventing, minimizing, and managing pain in patients with chronic wounds: challenges and solutions, *Chronic Wound Care Manag. Res.* 3 (2016) 85–90, <https://doi.org/10.2147/cwcmr.s85463>.
- [14] L.M. Morton, T.J. Phillips, Wound healing and treating wounds Differential diagnosis and evaluation of chronic wounds, *J. Am. Acad. Dermatol.* 74 (2016) 589–605, <https://doi.org/10.1016/j.jaad.2015.08.068>.
- [15] S. Tavadia, J. Bianchi, R.S. Dawe, M. McEvoy, E. Wiggins, E. Hamill, M. Urcelay, A. M.M. Strong, W.S. Douglas, Allergic contact dermatitis in venous leg ulcer patients, *Contact Dermatitis* 48 (2003) 261–265, <https://doi.org/10.1034/j.1600-0536.2003.00111.x>.
- [16] C. Berry-Kilgour, J. Cabral, L. Wise, Advancements in the delivery of growth factors and cytokines for the treatment of cutaneous wound indications, *Adv. Wound Care* 10 (2021) 596–622, <https://doi.org/10.1089/wound.2020.1183>.
- [17] P. Martin, Wound Healing-Aiming for Perfect Skin Regeneration, *Science* 276 (1997) 75–81. <http://science.sciencemag.org/> (accessed December 2, 2019).
- [18] R. Goldman, Growth factors and chronic wound healing : past , present , and future, *Adv. Skin Wound Care* 17 (2004).
- [19] H.S. Kim, X. Sun, J.-H. Lee, H.-W. Kim, X. Fu, K.W. Leong, Advanced drug delivery systems and artificial skin grafts for skin wound healing, *Adv. Drug Deliv. Rev.* (2018), <https://doi.org/10.1016/j.addr.2018.12.014>.
- [20] R. Fraioli, S. Neubauer, F. Rechenmacher, B.M. Bosch, K. Dashnyam, J.H. Kim, R. A. Perez, H.W. Kim, F.J. Gil, M.P. Ginebra, J.M. Manero, H. Kessler, C. Mas-Moruno, Control of stem cell response and bone growth on biomaterials by fully non-peptidic integrin selective ligands, *Biomater. Sci.* 7 (2019) 1281–1285, <https://doi.org/10.1039/c8bm01466c>.
- [21] M.S. Kang, N.H. Lee, R.K. Singh, N. Mandakbayer, R.A. Perez, J.H. Lee, H.W. Kim, Nanocements produced from mesoporous bioactive glass nanoparticles, *Biomaterials* 162 (2018) 183–199, <https://doi.org/10.1016/j.biomaterials.2018.02.005>.
- [22] K.D. Patel, T.H. Kim, N. Mandakbayer, R.K. Singh, J.H. Jang, J.H. Lee, H.W. Kim, Coating biopolymer nanofibers with carbon nanotubes accelerates tissue healing and bone regeneration through orchestrated cell- and tissue-regulatory responses, *Acta Biomater.* 108 (2020) 97–110, <https://doi.org/10.1016/j.actbio.2020.03.012>.
- [23] T.H. Kim, M.S. Kang, N. Mandakbayer, A. El-Fiqi, H.W. Kim, Anti-inflammatory actions of folate-functionalized bioactive ion-releasing nanoparticles imply drug-free nanotherapy of inflamed tissues, *Biomaterials* 207 (2019) 23–38, <https://doi.org/10.1016/j.biomaterials.2019.03.034>.
- [24] L. Kong, Z. Wu, H. Zhao, H. Cui, J. Shen, J. Chang, H. Li, Y. He, Bioactive injectable hydrogels containing desferrioxamine and bioglass for diabetic wound healing,

- ACS Appl. Mater. Interfaces 10 (2018) 30103–30114, <https://doi.org/10.1021/ACSAMI.8B09191>.
- [25] Z. Tu, Y. Zhong, H. Hu, D. Shao, R. Haag, M. Schirner, J. Lee, B. Sullenger, K. W. Leong, Design of therapeutic biomaterials to control inflammation, *Nat. Rev. Mater.* (2022), 0123456789, <https://doi.org/10.1038/s41578-022-00426-z>.
- [26] S. Zhao, L. Li, H. Wang, Y. Zhang, X. Cheng, N. Zhou, M.N. Rahaman, Z. Liu, W. Huang, C. Zhang, Wound dressings composed of copper-doped borate bioactive glass microfibers stimulate angiogenesis and heal full-thickness skin defects in a rodent model, *Biomaterials* 53 (2015) 379–391, <https://doi.org/10.1016/j.biomaterials.2015.02.112>.
- [27] A.K. Olaiya, S.T. Fadason, Studies on zinc and copper ion in relation to wound healing in male and female west african dwarf goats, *Niger. J. Physiol. Sci.* 31 (2016) 171–176. [www.njps.com.ng](http://www.njps.com.ng). (Accessed 24 May 2018).
- [28] T. Liu, B. Xiao, F. Xiang, J. Tan, Z. Chen, X. Zhang, C. Wu, Z. Mao, G. Luo, X. Chen, J. Deng, Ultrasmall copper-based nanoparticles for reactive oxygen species scavenging and alleviation of inflammation related diseases, *Nat. Commun.* 11 (11) (2020) 1–16, <https://doi.org/10.1038/s41467-020-16544-7>, 2020.
- [29] J. Xu, A. Nyga, W. Li, X. Zhang, N. Gavara, M.M. Knight, J.C. Shelton, Cobalt ions stimulate a fibrotic response through matrix remodelling, fibroblast contraction and release of pro-fibrotic signals from macrophages, *Eur. Cell. Mater.* 36 (2018) 142–155, <https://doi.org/10.22203/eCm.v036a11>.
- [30] S. Fu, H. Meng, F. Freer, J. Kwon, J.C. Shelton, M.M. Knight, Sub-toxic levels of Co<sup>2+</sup> are anti-inflammatory and protect cartilage from degradation caused by IL-1 $\beta$ , *Clin. Biomech.* 79 (2020) <https://doi.org/10.1016/j.clinbiomech.2019.12.006>.
- [31] H. Choudhury, M. Pandey, Y.Q. Lim, C.Y. Low, C.T. Lee, T.C.L. Marilyn, H.S. Loh, Y.P. Lim, C.F. Lee, S.K. Bhattamishra, P. Kesharwani, B. Gorain, Silver nanoparticles: advanced and promising technology in diabetic wound therapy, *Mater. Sci. Eng. C* 112 (2020), <https://doi.org/10.1016/j.msec.2020.110925>.
- [32] A.K. Solanki, H. Autefage, A.R. Rodriguez, S. Agarwal, J. Penide, M. Mahat, T. Whittaker, A. Nommeots-Nomm, E. Littmann, D.J. Payne, A.D. Metcalfe, F. Quintero, J. Pou, M.M. Stevens, J.R. Jones, Cobalt containing glass fibres and their synergistic effect on the HIF-1 pathway for wound healing applications, *Front. Bioeng. Biotechnol.* 11 (2023) 1–15, <https://doi.org/10.3389/fbioe.2023.1125060>.
- [33] A.K. Solanki, F.V. Lali, H. Autefage, S. Agarwal, A. Nommeots-Nomm, A. D. Metcalfe, M.M. Stevens, J.R. Jones, Bioactive glasses and electrospun composites that release cobalt to stimulate the HIF pathway for wound healing applications, *Biomater. Res.* 25 (2021) 1–16, <https://doi.org/10.1186/s40824-020-00202-6>.
- [34] A.G.S. de Laia, T.M. Valverde, B.R. Barrioni, P. da S. Cunha, A.M. de Goes, M.C. de Miranda, D.A. Gomes, C.M. Queiroz-Junior, M.A. de Sá, M. de Magalhães Pereira, Cobalt-containing bioactive glass mimics vascular endothelial growth factor A and hypoxia inducible factor 1 function, *J. Biomed. Mater. Res., Part A* 109 (2021) 1051–1064, <https://doi.org/10.1002/jbm.a.37095>.
- [35] Z. Azari, S. Nazarnezhad, T.J. Webster, S.J. Hoseini, P. Brouki Milan, F. Baino, S. Kargozar, Stem cell-mediated angiogenesis in skin tissue engineering and wound healing, *Wound Repair Regen.* 30 (2022) 421–435, <https://doi.org/10.1111/wrr.13033>.
- [36] N. Mandakhbayar, A. El-Fiqi, K. Dashnyam, H. L. H.-W.K. Khandmaa Dashnyam, Jung-Hwan Lee, Nandin Mandakhbayar, Guang-Zhen Jin, Feasibility of defect tunable bone engineering using electroblown bioactive fibrous scaffolds with dental stem cells, *ACS Biomater. Sci. Eng.* (2018), <https://doi.org/10.1021/acsbomaterials.7b00810>.
- [37] K. Dashnyam, A. El-Fiqi, J.O. Buitrago, R.A. Perez, J.C. Knowles, H.W. Kim, A mini review focused on the proangiogenic role of silicate ions released from silicon-containing biomaterials, *J. Tissue Eng.* 8 (2017), 204173141770733, <https://doi.org/10.1177/2041731417707339>.
- [38] A. El-Fiqi, H.W. Kim, Sol-gel synthesis and characterization of novel cobalt ions-containing mesoporous bioactive glass nanospheres as hypoxia and ferroptosis-inducing nanotherapeutics, *J. Non-Cryst. Solids* 569 (2021), 120999, <https://doi.org/10.1016/j.jnoncrysol.2021.120999>.
- [39] V.K. Tripathi, S.A. Subramanian, I. Hwang, Molecular and cellular response of Co-cultured cells toward cobalt chloride (CoCl<sub>2</sub>)-Induced hypoxia, *ACS Omega* (2019), <https://doi.org/10.1021/acsomega.9b01474>.
- [40] Z. Deng, B. Lin, Z. Jiang, W. Huang, J. Li, X. Zeng, H. Wang, D. Wang, Y. Zhang, Hypoxia-mimicking cobalt-doped borosilicate bioactive glass scaffolds with enhanced angiogenic and osteogenic capacity for bone regeneration, *Int. J. Biol. Sci.* 15 (2019) 1113–1124, <https://doi.org/10.7150/ijbs.32358>.
- [41] K. Boldbaatar, K. Dashnyam, J.C. Knowles, H.H. Lee, J.H. Lee, H.W. Kim, Dual-ion delivery for synergistic angiogenesis and bactericidal capacity with silica-based microsphere, *Acta Biomater.* 83 (2019) 322–333, <https://doi.org/10.1016/j.actbio.2018.11.025>.
- [42] H. Thangarajah, D. Yao, E.I. Chang, Y. Shi, L. Jazayeri, I.N. Vial, R.D. Galiano, X.-L. Du, R. Grogan, M.G. Galvez, M. Januszyk, M. Brownlee, G.C. Gurtner, The molecular basis for impaired hypoxia-induced VEGF expression in diabetic tissues, *PNAS*. 106 (2009) 13505–13510. [www.pnas.org/cgi/content/full/](http://www.pnas.org/cgi/content/full/). (Accessed 6 September 2019).
- [43] A.P. Veith, K. Henderson, A. Spencer, A.D. Sliagar, A.B. Baker, Therapeutic strategies for enhancing angiogenesis in wound healing, *Adv. Drug Deliv. Rev.* (2018), <https://doi.org/10.1016/j.addr.2018.09.010>.
- [44] H. Thangarajah, I.N. Vial, R.H. Grogan, D. Yao, Y. Shi, M. Januszyk, R.D. Galiano, E.I. Chang, M.G. Galvez, J.P. Glotzbach, V.W. Wong, M. Brownlee, G.C. Gurtner, HIF-1 $\alpha$  dysfunction in diabetes, *Cell Cycle* 9 (2010) 75–79, <https://doi.org/10.4161/cc.9.1.10371>.
- [45] Y. Wang, R. Xu, G. Luo, Q. Lei, Q. Shu, Z. Yao, H. Li, J. Zhou, J. Tan, S. Yang, R. Zhan, W. He, J. Wu, Biomimetic fibroblast-loaded artificial dermis with “sandwich” structure and designed gradient pore sizes promotes wound healing by favoring granulation tissue formation and wound re-epithelialization, *Acta Biomater.* 30 (2016) 246–257, <https://doi.org/10.1016/j.actbio.2015.11.035>.
- [46] M. Gao, T.T. Nguyen, M.A. Suckow, W.R. Wolter, M. Gooyit, S. Mobashery, M. Chang, Acceleration of diabetic wound healing using a novel protease-anti-protease combination therapy, *Proc. Natl. Acad. Sci. USA* 112 (2015) 15226–15231, <https://doi.org/10.1073/pnas.1517847112>.
- [47] Y. Liu, Y. Cheng, H. Zhang, M. Zhou, Y. Yu, S. Lin, B. Jiang, X. Zhao, L. Miao, C. W. Wei, Q. Liu, Y.W. Lin, Y. Du, C.J. Butch, H. Wei, Integrated cascade nanzyme catalyzes in vivo ROS scavenging for anti-inflammatory therapy, *Sci. Adv.* 6 (2020), <https://doi.org/10.1126/sciadv.abb2695>.
- [48] H. Wu, F. Li, S. Wang, J. Lu, J. Li, Y. Du, X. Sun, X. Chen, J. Gao, D. Ling, Ceria nanocrystals decorated mesoporous silica nanoparticle based ROS-scavenging tissue adhesive for highly efficient regenerative wound healing, *Biomaterials* 151 (2018) 66–77, <https://doi.org/10.1016/j.biomaterials.2017.10.018>.
- [49] C.M. Oliveira Volpe, P. Henrique Villar-Delfino, P.M. Ferreira Dos Anjos, J.A. Nogueira-Machado, Cellular death, reactive oxygen species (ROS) and diabetic complications, *Cell Death and Disease*. 9119 (2018) 2–9. <https://doi.org/10.1038/s41419-017-0135-z>.
- [50] Z. Tu, M. Chen, M. Wang, Z. Shao, X. Jiang, K. Wang, Z. Yao, S. Yang, X. Zhang, W. Gao, C. Lin, B. Lei, C. Mao, Engineering bioactive M2 macrophage-polarized anti-inflammatory, antioxidant, and antibacterial scaffolds for rapid angiogenesis and diabetic wound repair, *Adv. Funct. Mater.* (2021), 2100924, <https://doi.org/10.1002/adfm.202100924>, 1–18.
- [51] J. Xu, J. Yang, A. Nyga, M. Ehteramy, A. Moraga, Y. Wu, L. Zeng, M.M. Knight, J. C. Shelton, Cobalt (II) ions and nanoparticles induce macrophage retention by ROS-mediated down-regulation of RhoA expression, *Acta Biomater.* 72 (2018) 434–446, <https://doi.org/10.1016/j.actbio.2018.03.054>.
- [52] D. Shweiki, A. Itin, D. Soffer, E. Keshet, Vascular endothelial growth factor induced by hypoxia may mediate hypoxia-initiated angiogenesis, *Nature* 359 (1992) 843–845, <https://doi.org/10.1038/359843a0>.
- [53] S. Oladipupo, S. Hu, J. Kovalski, J. Yao, A. Santeford, R.E. Sohn, R. Shohet, K. Maslov, L. V Wang, J.M. Arbeit, VEGF is essential for hypoxia-inducible factor-mediated neovascularization but dispensable for endothelial sprouting, *Proc. Natl. Acad. Sci. USA* (2011), <https://doi.org/10.1073/pnas.1101321108>.
- [54] X. Gao, S. Ma, X. Xing, J. Yang, X. Xu, C. Liang, Y. Yu, L. Liu, L. Liao, W. Tian, Microvessels derived from hiPSCs are a novel source for angiogenesis and tissue regeneration, *J. Tissue Eng.* 13 (2022), <https://doi.org/10.1177/20417314221143240>.
- [55] L. Nalbach, D. Müller, S. Wrublewsky, W. Metzger, M.D. Menger, M.W. Laschke, E. Ampof, Microvascular fragment spheroids: three-dimensional vascularization units for tissue engineering and regeneration, *J. Tissue Eng.* 12 (2021), <https://doi.org/10.1177/20417314211035593>.
- [56] C.N. Tchanque-Fossuo, S.E. Dahle, S.R. Buchman, R. Rivkah Isseroff, Deferoxamine: potential novel topical therapeutic for chronic wounds, *Br. J. Dermatol.* 176 (2017) 1056–1059, <https://doi.org/10.1111/bjd.14956>.
- [57] J.H. Lee, A. El-Fiqi, N. Mandakhbayar, H.H. Lee, H.W. Kim, Drug/ion co-delivery multi-functional nanocarrier to regenerate infected tissue defect, *Biomaterials* 142 (2017) 62–76, <https://doi.org/10.1016/j.biomaterials.2017.07.014>.
- [58] G.T.-J. Huang, W. Sonoyama, J. Chen, S.H. Park, In vitro characterization of human dental pulp cells: various isolation methods and culturing environments, *Cell Tissue Res.* 324 (2006) 225–236, <https://doi.org/10.1007/s00441-005-0117-9>.
- [59] N. Mandakhbayar, A. El-Fiqi, J.H. Lee, H.W. Kim, Evaluation of strontium-doped nanobioactive glass cement for dentin-pulp complex regeneration therapy, *ACS Biomater. Sci. Eng.* 5 (2019) 6117–6126, <https://doi.org/10.1021/acsbomaterials.9b01018>.
- [60] K. Dashnyam, G.Z. Jin, J.H. Kim, R. Perez, J.H. Jang, H.W. Kim, Promoting angiogenesis with mesoporous microcarriers through a synergistic action of delivered silicon ion and VEGF, *Biomaterials* 116 (2017) 145–157, <https://doi.org/10.1016/j.biomaterials.2016.11.053>.
- [61] B.L. Furman, Streptozotocin-induced diabetic models in mice and rats, *Curr. Protoc. Pharmacol.* 70 (2015), <https://doi.org/10.1002/0471141755.ph0547s70>, 5.47.1–5.47.20.
- [62] K.K. Wu, Y. Huan, Streptozotocin-induced diabetic models in mice and rats, *Curr. Protoc. Pharmacol.* (2008) 1–14, <https://doi.org/10.1002/0471141755.ph0547s40>.
- [63] a Gajdosíková, a Gajdosíková, M. Stefek, J. Navarová, R. Hozová, Streptozotocin-induced experimental diabetes in male Wistar rats, *Gen. Physiol. Biophys.* 18 (1999) 54–62. *Spec No.*
- [64] L. Liu, G.P. Marti, X. Wei, X. Zhang, H. Zhang, Y. V. Liu, G.L. Semenza, J. W. Harmon, L. Jing, S. Li, Q. Li, M.R. Dasu, I. Jialal, A. Ahluwalia, A.S. Tarnawski, M. Ecol, M.R. Dasu, S.J. Martin, Toll-like receptor expression and signaling in human diabetic wounds, *Exp. Ther. Med.* 9 (2014) 2141–2146, <https://doi.org/10.1111/mec.13536>.Application.